International Journal of Aerospace Engineering

Dynamics and Control of Distributed Space Systems

Lead Guest Editor: Chuang Liu
Guest Editors: Keke Shi, Neng Wan, and Xiaokui Yue

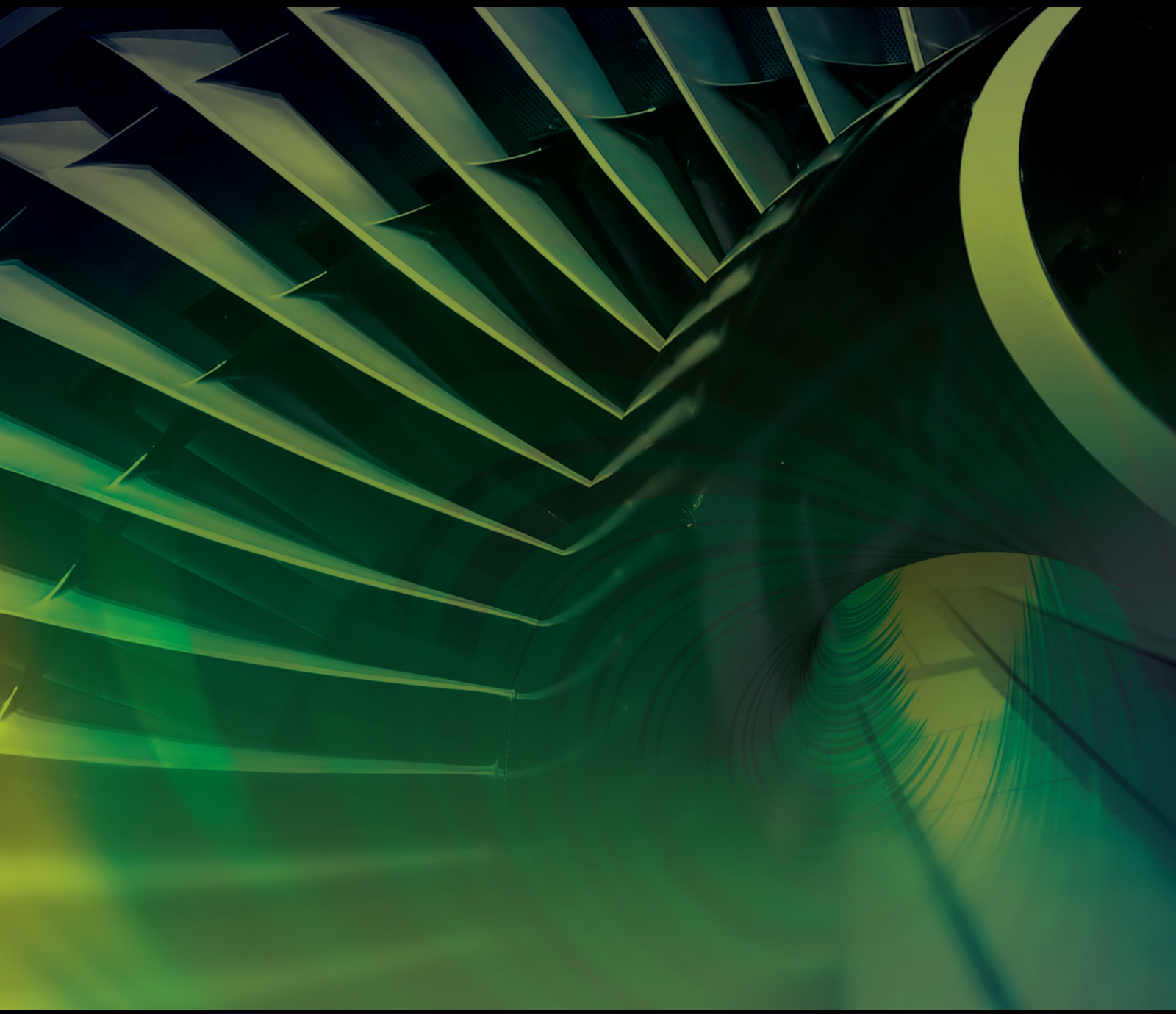

Dynamics and Control of Distributed Space Systems

International Journal of Aerospace Engineering

Dynamics and Control of Distributed Space Systems

Lead Guest Editor: Chuang Liu
Guest Editors: Keke Shi, Neng Wan, and Xiaokui Yue

Copyright © 2022 Hindawi Limited. All rights reserved.

This is a special issue published in “International Journal of Aerospace Engineering.” All articles are open access articles distributed under the Creative Commons Attribution License, which permits unrestricted use, distribution, and reproduction in any medium, provided the original work is properly cited.

Chief Editor

Dan Zhao, New Zealand

Associate Editors

Jiaqiang E., China
Mahmut Reyhanoglu, USA
Paul Williams, The Netherlands

Academic Editors

José Ángel Acosta, Spain
Giulio Avanzini, Italy
Franco Bernelli-Zazzera, Italy
Debes Bhattacharyya, New Zealand
Paolo Castaldi, Italy
Enrico Cestino, Italy
Hao Chen, China
Jinchao Chen, China
Pengyun Chen, China
Gautam Choubey, India
Christian Circi, Italy
Antonio Concilio, Italy
Giovanni Delibra, Italy
Hongbing Ding, China
Juan Du, China
Juan-Antonio Escareno, France
Ke Feng, Canada
Fangzhou Fu, China
Qingfei Fu, China
Paolo Gasbarri, Italy
Adel Ghenaiet, Algeria
Tuo Han, China
Shaoming He, China
Santiago Hernández, Spain
Robert W. Hewson, United Kingdom
Ratneshwar Jha, USA
Erkan Kayacan, Australia
Jun-Wei Li, China
Xiaobin Lian, China
Aqiang Lin, China
William W. Liou, USA
Chuang Liu, China
Francisco Ronay Lopez Estrada, Mexico
Enrico C. Lorenzini, Italy
Maj D. Mirmirani, USA
Marco Morandini, Italy
Muhammad Rizwan Mughal, Oman
Giovanni Palmerini, Italy
Dario Pastrone, Italy
Rosario Pecora, Italy
Marco Pizzarelli, Italy
Seid H. Pourtakdoust, Iran
Vijayanandh Raja, India
Fabio Santoni, Italy
Manigandan Sekar, India
Jacopo Serafini, Italy
Zhiguang Song, China
Jeremy Straub, USA
Dakun Sun, China
Mohammad Tawfik, Egypt
Zhen-Yu Tian, China
Linda L. Vahala, USA
Guillermo Valencia-Palomo, Mexico
Eusebio Valero, Spain
Antonio Viviani, Italy
Gang Wang, China
Yue Wang, China
Liqiu Wei, China
Shunan Wu, China
Hao Xia, United Kingdom
Kan Xie, China
Binbin Yan, China
Xianfeng Yang, China
Changxiao ZHAO, China
Alex Zanotti, Italy
Mustafa Zeybek, Turkey
J Zhang, China
Rong-Chun Zhang, China

Contents

Performance Improvement for Single-Photon LiDAR with Dead Time Selection
Lei Feng, Fenglin Wang, Meng An, and Qiang Zhang
Research Article (9 pages), Article ID 6847331, Volume 2022 (2022)

Maneuver Strategy for Active Spacecraft to Avoid Space Debris and Return to the Original Orbit
Qun Fang, Zhen Zhang, Haodong Meng, Xiaolong Wang, and Xiuwei Zhang
Research Article (16 pages), Article ID 4650730, Volume 2022 (2022)

Hindawi
International Journal of Aerospace Engineering
Volume 2022, Article ID 6847331, 9 pages
https://doi.org/10.1155/2022/6847331

Research Article

Performance Improvement for Single-Photon LiDAR with Dead Time Selection

Lei Feng,[1] **Fenglin Wang**,[1] **Meng An**,[2] **and Qiang Zhang**[2]

[1]*Beijing Institute of Tracking and Telecommunication Technology, Beijing 100094, China*
[2]*Institute of Spacecraft System Engineering CAST, Beijing 100094, China*

Correspondence should be addressed to Lei Feng; fenglei_798@163.com

Received 1 April 2022; Revised 7 May 2022; Accepted 31 May 2022; Published 1 July 2022

Academic Editor: Keke Shi

Copyright © 2022 Lei Feng et al. This is an open access article distributed under the Creative Commons Attribution License, which permits unrestricted use, distribution, and reproduction in any medium, provided the original work is properly cited.

Compared with the impulse LiDAR, the single-photon LiDAR has higher measurement sensitivity in the prominent feature, especially for space-based long-distance imaging. The distance measurement and the detection probability are the critical performance for LiDAR. The ranging of single-photon LiDAR is mainly different from the photon ranging of pulsed LiDAR. Dead time has a significant effect on distance measurement accuracy and detection probability, which are key parameters for detectors when implementing sound control. Therefore, the model of detector dead time, measurement accuracy, and detection probability should be established, and simulation results that meet application requirements should be achieved. Based on the single-photon ranging theory, the dead time, measurement accuracy, and detection probability model of single-photon LiDAR are studied. Furthermore, the systematic simulation of different contrasts is carried out according to the model. The simulation results demonstrate that the model can accurately perform the relationship between dead time and single-photon LiDAR system parameters. The research results can prove the design and verification of single-photon LiDAR dead time.

1. Introduction

The traditional space-based LiDAR ranging uses a linear pulse detection system with low detection sensitivity. It relies on a high threshold-to-noise ratio to distinguish the echo signal from the background noise. Hence, the required laser energy aperture product is significantly large. The laser echo pulse contains at least thousands of photons of energy [1]. On the one hand, the high laser emission energy limits the repetition frequency of the emitted laser, the data sampling rate, and the detection distance. On the other hand, a large number of echo photons are wasted. The advantage of photon-counting laser ranging technology is that it can obtain distance information of long-distance targets with lower laser pulse energy, thereby increasing the number of beams, reducing the system's requirements for space-based satellite platforms such as power consumption and telescope aperture, and improving system performance, time resolution accuracy, and detection accuracy. The single-photon multimode LiDAR detector adopts a new single-photon system with the detector output energy according to photons [2]. The single-photon detection efficiency and dark count are determined by the dead time of the system. Thus, the dead time of the single-photon detector directly affects the detection of the system. Efficiency and dark count size will ultimately affect the bit error rate, affecting system indicators such as LiDAR detection probability and ranging accuracy.

It is worth noting that the single-photon LiDAR can be used for relative position and velocity control in spacecraft rendezvous and docking with high precision, which can also be adopted in distributed space systems, e.g., satellite constellation, satellite swarm, and federated satellite, including many satellites distributed in different orbits cooperating with each other to perform a very complex space mission [3–5]. However, the measurement of single-photon LiDAR may cause measurement errors or input delay. After docking, for combined spacecraft attitude control problem with the unknown measurement delay and input delay, the work in [6] investigated a novel intermediate-observer to achieve effective stabilization. Nevertheless, the time-delay was only considered, such that the application of this approach was relatively conservative. Much literature has made great

contributions to spacecraft control, most of which depends on that the state information can be known exactly and applied to control instructions directly. In fact, the single-photon LiDAR can make sense to provide the state information [7–9].

In this paper, according to the working principle of single-photon detection, the relationship model between the dead time of the single-photon detector, ranging accuracy, and detection probability is established, and the correctness of the relationship model is verified by simulation under different contrasts. Finally, combined with the free-form surface spectroscopy system, simulations verify the relationship between dead time and probe illumination. The simulation results show that the relational model proposed in this paper can be applied to the determination of the dead time of the single-photon LiDAR detector and the design and verification of the index control.

2. Principle Analysis of Single-Photon Laser Detection

The schematic diagram of the working principle for single-photon laser detection is shown in Figure 1.

Single-photon LiDAR is a photon-counting system. The system completes laser ranging through photon counting [10]. Based on pulsed laser ranging, the introduction of time correlation conforms to single-photon counting, and the linear detection system contains many photons. The detection of the echo waveform is converted into a count for a single echo photon event, making full use of the single-photon level energy in the echo signal, using the correlation of the target distance information and the cumulative count of photon events in the background noise and dark counts. The actual distance data is extracted to improve the detection probability and maximize the system's detection sensitivity and efficiency. The histogram statistics of photon event detection of echo signal based on time correlation are shown in Figure 2. In this figure, the abscissa is the number of single-photon events and the number of transmitted pulses, and the ordinate is the ranging elevation accuracy.

Unlike the imaging method of CCD or CIS image sensor that is usually used in traditional LiDAR to read the sound charge, single-photon LiDAR generally uses a single-photon avalanche diode [11]. After the array is integrated, the ranging function is realized.

A single-photon avalanche diode is an avalanche photodiode that operates in the Geiger mode [12, 13]. A continuous avalanche breakdown occurs when photons strike the active region of the diode, so a quench circuit is required to stop the avalanche process. Therefore, the output voltage from the avalanche to the end of quenching appears as a single pulse signal one after the other, and one pulse corresponds to one photon. The periodic pulse signal can be output as a pulse square wave signal one by one after the shaping circuit, and the counter can record the number. The light intensity can be quantified by counting the number of pulses, and a detector array composed of multiple single-photon avalanche diodes can be used as a detection device.

3. Dead Time Impact Analysis

Many factors affect the ranging accuracy of single-photon LiDAR, and the modeling process is complicated. The main factors related to single-photon detectors are the influence of the dead time of the avalanche diode on the effective receiving aperture modeling and the dead time of the detector on the ranging accuracy [14].

3.1. Detector Dead Time Effect on the Effective Receiver Aperture. For each laser pulse detection, the existence of any dead time will limit the number of signal photon events [15]. Suppose the receiver dead time τ_d is greater than the signal photon distribution time τ_s, less than the time corresponding to the distance sampling interval τ_b, and the number of signal photons reaches the upper limit. The contrast ratio is shown in the following formula:

$$\lim_{n_s \gg 1} C_d = 1 - \frac{\tau_d}{\tau_b} + \frac{1}{n_b}. \tag{1}$$

In the above formula, C_d is the contrast when the number of signal photons reaches the upper limit, n_s is the average number of signal photons, n_b is the average number of photons sampled for each distance, τ_d is the receiver dead time, and τ_b is the time corresponding to the distance sampling interval. When the dead time of the detector or receiver exceeds the distribution of echo signal photons, only one photon in the signal photon stream can be effectively detected, and any redundant signal photons cannot be detected [16]. Due to the existence of the received dead time, when the extreme situation occurs, that is, the signal photon appears within the dead time range of the detector, the signal photon will not be detected at this time, and the noise photon that triggers the detector will be the signal photon event by default. It brings a sizeable ranging error [17]. Since each pixel works independently and does not affect each other for multielement detectors, more signal photons can be obtained in a single laser pulse. The utilization rate of signal photons is significantly increased. At the same time, the background noise photons are distributed to more pixels. When designing the system, the aperture of the leading optical component of the receiver can be appropriately increased, which reduces the requirement for the single-pulse energy of the transmitter [18]. Using a multielement single-photon detector, the maximum allowable effective receiving area is shown in

$$\begin{aligned} A_r &= \frac{1}{\beta/N_P\left[\tau_b C_d - 1/1 - \exp\left(-n_s/N_p\right) + \tau_d\right]} \\ &\approx \frac{N_1}{\beta\tau_b\left[(C_d - 1) + (1 - e^{-n_p})\tau_d/\tau_b\right]}. \end{aligned} \tag{2}$$

In formula (2), A_r is the maximum allowable effective receiving area, C_d is the contrast when the number of signal photons reaches the upper limit, n_s is the average number of signal photons, τ_d is the receiver dead time, τ_s is the signal photon distribution time, and τ_b is the time corresponding

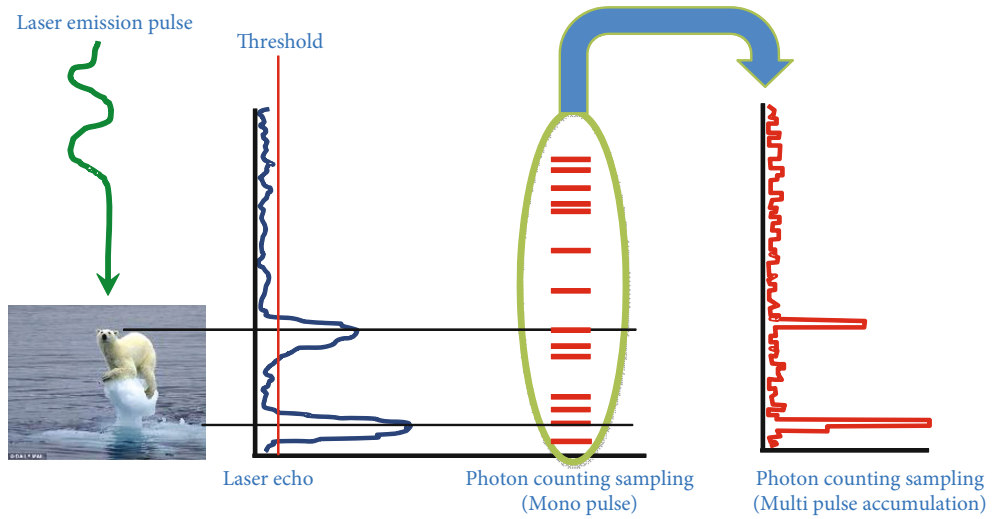

Figure 1: Operation schematic diagram for single-photon laser detection.

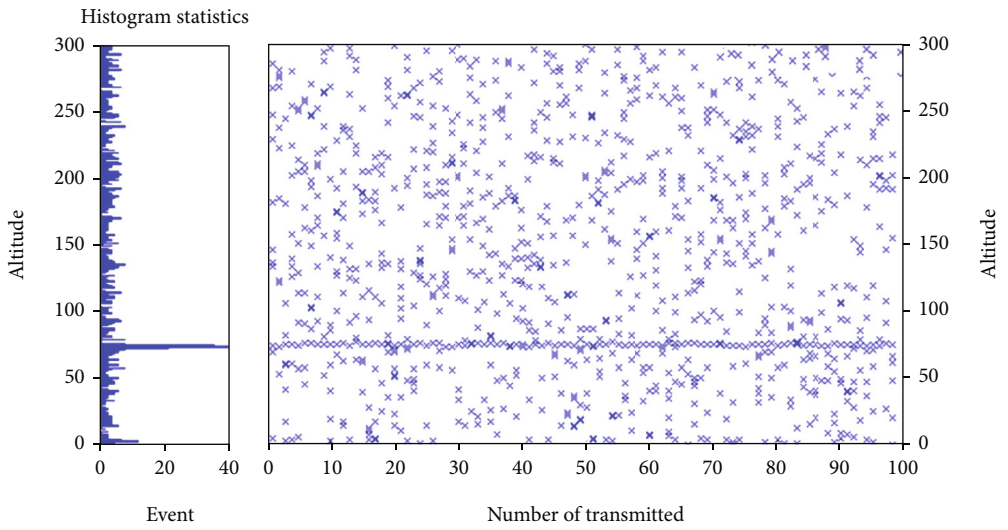

Figure 2: Statistical histogram for time-related back wave signal photon event detection.

to the distance sampling interval. β is the composite noise count rate per unit area of the receiver, N_p is the number of pixels received by the detector, and N_1 is the signal photon count event acquired by the detector. $N_1 \approx N_p(1 - e^{-n_p})$, within $n_p = n_s/N_p$, n_s is the number of signal photons incident on the photosensitive surface of the detector. The modeling and simulation of the unit detector and the 16-element detector are carried out. Assuming that the receiver dead time is 16 ns and the average signal photon number is 6, the relationship between the effective receiving aperture of the main optical component of the receiver and the signal contrast is shown in Figure 3.

Figure 3 is the dead time of the unit detector and the 16-element detector receiver, respectively. Under the condition of the average number of signal photons $n_s = 6$, when the system adopts unit detectors and multielement detectors, the simulation results of the relationship between the maximum allowable effective receiving aperture of the receiver and the signal contrast show that with the increase of the number of detector elements, under the same signal contrast, the required practical receiving the size of the caliber becomes more significant, and the same model relationship is satisfied.

At the same time, under the condition that the signal contrasts are $C = 2, 3, 5, 10$, respectively, this paper analyzes the relationship between the effective receiving aperture of the optical component and the receiving dead time of the detector as shown in Figure 4.

Figure 4 shows the relationship between the maximum allowable effective receiving aperture of the receiver and the signal contrast when the system uses a unit detector and a multielement detector under the condition that the signal contrasts are $C = 2, 3, 5, 10$, respectively. Through simulation analysis, to ensure the same signal contrast, multielement detectors can increase the allowable receiving area by about 4-6 times compared with single-pixel detectors.

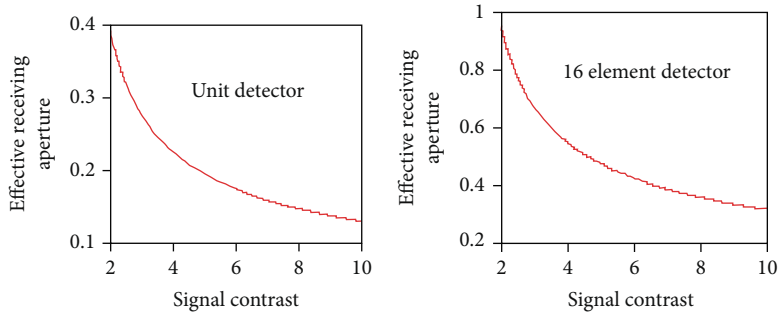

Figure 3: Contrast and effective aperture for single-pixel detector and 16 detectors.

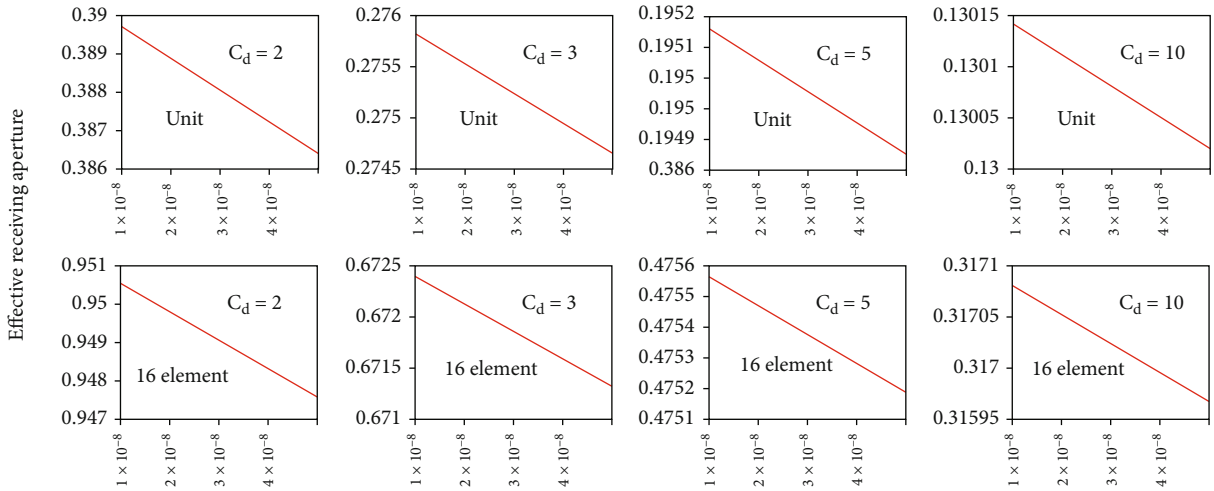

Figure 4: LiDAR receiver dead time and effective receive aperture relationship.

According to the above analysis, for example, the dead time of the detector is 16 ns, the number of pixels is 16, and the contrast is 3. According to the maximum aperture constraint, the aperture is 1000 mm.

3.2. The Detector Dead Time Influence on Ranging Accuracy. The dead time of the LiDAR receiver directly affects the ranging accuracy of the integrated load system. To reduce the impact of dead time on ranging accuracy, it is necessary to integrate the photosensitive surface of each single-photon detector into its detection circuit [19–21]. By receiving 4×4 pixels of a single laser footprint, the dead time of the detection link is reduced, the limitation of the dead time on the receiving aperture is also reduced, and the ranging accuracy is improved. Assuming that the number of multibeam ranging channels is 1000, the size of the detection array is 4000×4. The pixel assignment is shown in Figure 5.

In the working process of LiDAR, the echo pulse width is widened due to the influence of beam divergence angle, ground slope, and roughness. The widening effect is more pronounced if the measurement object is a cloud, tree canopy, and other penetrating targets or soft targets. The probability that the signal photon triggers the photon detector in the time range $f(\tau, \tau + d\tau)$ is equal to the product of the detection probability in the unit time range and the probability that it is not triggered in the previous unit time range, as shown in

$$P(\tau)d\tau = C_N s(\tau)d\tau \left\{ \int_{\tau-\tau_d}^{\tau} d\tau' s\left(\tau'\right) \right\}, \tag{3}$$

where $\tau = t - 2h_0/c$ is the difference between the pulse emission time and the optical path time reaching the center of the beam. h_0 is the optical path of the pulse to the center of the beam. $s(\tau)$ is the signal waveform arriving at the detector (or it can be more accurately defined as the Poisson generation function). C_N is the detection probability, and τ_d is the receiver dead time. The contribution of detector pixels to small noise counting events in the echo pulse time domain is not considered in (3). The contribution of background noise events to the whole photon-counting event is limited to one distance sampling interval. The system deviation and ranging accuracy for the unit detector are expressed as follows:

$$\begin{aligned} \langle \Delta R \rangle &= \frac{C}{2} \langle \tau \rangle, \\ \Delta R_{\mathrm{RMS}} &= \frac{C}{2} \sqrt{\langle \tau^2 \rangle - \langle \tau \rangle^2}, \end{aligned} \tag{4}$$

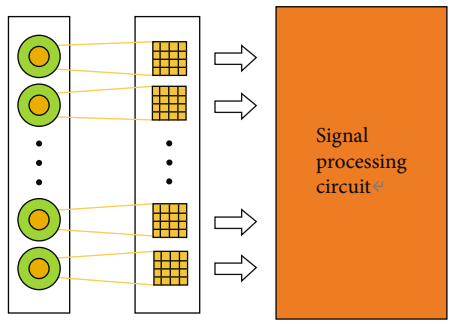

Figure 5: Size of the single-photon detector.

where $\langle \Delta R \rangle$ is the systematic deviation, ΔR_{RMS} is the root mean square of system ranging accuracy, and $\langle \tau \rangle$ and $\langle \tau^2 \rangle$ are the average value and mean square value of pulse broadening probability distribution in (3), respectively. Relative to pulse broadening, for extreme cases where the dead time is very small ($\tau_d \ll \tau_c$) or very large ($\tau_d \gg \tau_c$), the specific form is shown in

$$P_0(\tau)d\tau = \frac{1}{n_s} s(\tau)d\tau, \tag{5}$$

$$P_\infty(\tau)d\tau = \frac{1}{1-e^{-n_s}} d\tau \cdot s(\tau) \cdot \exp\left\{-\int_{-\infty}^{\tau} d\tau' s\left(\tau'\right)\right\}, \tag{6}$$

where $P_0(\tau)d\tau$ is the probability of triggering the photon detector within the time range of $(\tau, \tau + d\tau)$ when the dead time is very small ($\tau_d \ll \tau_c$), $P_\infty(\tau)d\tau$ is the probability of triggering the photon detector within the time range of $(\tau, \tau + d\tau)$ when the dead time is very large ($\tau_d \gg \tau_c$), n_s is the number of photon signals, and $s(\tau)$ is the signal waveform arriving at the detector.

Equation (5) defines a case where the first photon of the echo pulse triggers the receiver, and the other photons cannot be triggered normally due to the limitation of the dead time of the receiver. In the case of a weak echo signal ($n_s \ll 1$), the dead time of the detector is no longer a restrictive factor because the detector is triggered by an event with a small number of photons in the previous signal. In formula (6), the probability function of photon detection is closely related to the waveform, so the accurate identification time of echo is the center of the waveform. For the receiving system with a very small dead time or no dead time limit, in the case of a weak echo signal, the identification error of echo time tends to 0, which is independent of echo intensity. On the other hand, for the case of a large ground slope in the laser spot, due to the large deviation of the echo pulse distribution from the waveform center, the mean square error of the identification time is relatively large, especially the error introduced by the satellite attitude. Due to the exponential term in (3), the existence of the dead time of the LiDAR receiver will lead to the asymmetric effect of the photon detection probability function. The photon trigger detector with front distribution will increase the identification error of negative time when the echo signal is a strong echo signal. When the dead time exceeds 20 ns, this effect will lead to the sharp deterioration of ranging accuracy, which cannot reach the centimeter ranging accuracy.

Using the multipixel detector array and multichannel signal processor for parallel processing, the signal photon count and noise count of each detection pixel can be significantly reduced, and the dead time effect of each channel can be reduced. Using the above two measures, the time-domain broadening effect introduced by the single-pixel detector can be significantly reduced, so as to effectively reduce the ranging system error and ranging error.

4. Simulation Analysis

4.1. Simulation of the Single-Photon LiDAR Detection Probability. The requirements of detection probability are usually related to the setting of signal contrast, receiving aperture, dead receiver time, data frame period, and distance sampling interval. When allocating system indicators, it is necessary to select the combined working conditions of signal contrast and data frame period according to specific terrain, reflectivity, and other conditions under meeting ranging accuracy. Then, select the distance sampling interval and design the load system that can meet the requirements of detection probability. Single-photon measurement based on temporal and spatial correlation coincidence is adopted. Its detection probability is mainly expanded for photon-counting events of the detection signal in the data frame. The probability of successfully identifying and acquiring the signal detection unit in a given data frame is given by

$$P_{\mathrm{acq}} = P(N_t \geq K) = 1 - e^{-N_t} \sum_{t=0}^{K-1} \frac{{N_t}^K}{K!} = 1 - e^{-CN_b} \sum_{b=0}^{K-1} \frac{(CN_b)^K}{K!}, \tag{7}$$

where N_t is the number of photon events received by the detector within a data frame and K is the data frame discrimination threshold. Similarly, the probability of erroneously identifying the noise detection unit as a signal unit is as follows:

$$P_{\mathrm{false}} = P(N_b \geq K) = 1 - e^{-N_b} \sum_{b=0}^{K-1} \frac{{N_b}^K}{K!}. \tag{8}$$

In each frame, the number of noise detection units incorrectly identified as signal detection units is given as follows:

$$N_{\mathrm{false}} = N_{\mathrm{bin}} P_{\mathrm{false}}, \tag{9}$$

where $N_{\mathrm{bin}} = \tau_g / \tau_b$ is the number of sampling intervals within the distance gate, τ_g is the echo gate width, and τ_b is the distance sampling interval. Define the statistical probability difference of the detection unit, that is, the average expected value obtained by the signal unit minus the average

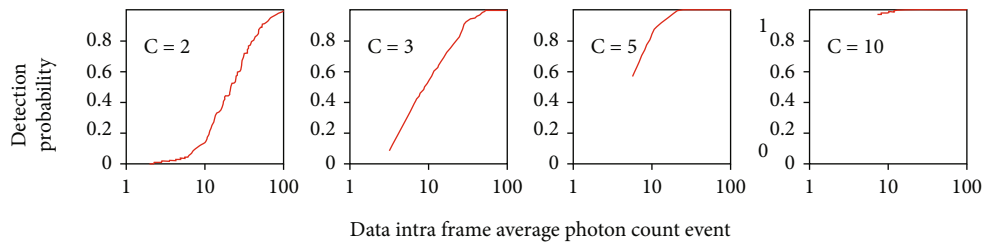

Figure 6: Relationship between detection probability and average photon-counting events inside the data frame.

Table 1: Effect analysis on signal detection for photon counting under given contrast.

Serial number	Target contrast	Data intraframe signal photon count	Detection probability	False alarm probability
1	2	80	0.999	7.664×10^{-6}
2	3	50	0.999	1.416×10^{-5}
3	5	35	0.999	8.653×10^{-6}
4	10	25	0.999	1.615×10^{-5}

expected value of the error acquisition noise unit as follows:

$$N(k) = P_{\text{acq}} - N_{\text{bin}} P_{\text{false}} = 1 - C^{\text{Kopt}} e^{-(C-1)N_b} - e^{-CN_b} \sum_{k=0}^{\text{Kopt}-1} \frac{(C^k - C^{\text{Kopt}}) N_b{}^k}{K!}, \quad (10)$$

where C^{Kopt} is optimal contrast and C^k is contrast under the data frame discrimination threshold. If the frame count threshold K is too small, too many noise detection units will be recognized as signal detection units, resulting in too small statistical probability difference of detection units ($\ll 1$) or even negative values. If the frame count threshold K is too large, the recognition algorithm will filter out too many signal photons, which will cause the statistical difference of the detection unit to be less than 1. During system design, this value needs to be selected to ensure the maximum difference in statistical probability of LiDAR detection. The relationship between the detection probability of the signal detection unit and the average photon-counting event in the data frame is shown in Figure 6 with $C = 2, 3, 5, 10$.

Different combinations of contrast and signal photon-counting events are simulated to distinguish the relationship between the detection probability in the data frame and the average photon-counting event in the data frame, as shown in Table 1. The simulation results show that the detection probability of LiDAR can reach 0.999 under several common imaging conditions in orbit. The false alarm probability reaches the lowest when the target contrast is two and the photon count value of the signal in the data frame is 80. When the target contrast is ten and the photon count value of the signal in the data frame is 25, the false alarm probability reaches the highest, which is 8.653×10^{-6}.

4.2. Simulation of the Single-Photon LiDAR Detection Illuminance. The detection illuminance of LiDAR needs to be simulated after the combination of beam homogenization and shaping system. The simulation verification method adopts the free-form surface to realize the beam homogenization, shaping, and emission. The combination of beam homogenization and shaping can realize the linear beam emission with uniform light intensity and ensure the slight divergence angle of the laser line in the transverse direction. Suppose the incident beam is a Gaussian beam and the target beam is a "linear" uniform distribution. They can be separated from variables; that is, $I_{\text{in}}(x, y)$ and $I_t(x', y')$ can be regarded as the product of two orthogonal one-dimensional illumination distributions: $I_{\text{in}}(x, y) = I_{\text{in},x}(x)$ $I_{\text{in},y}(y)$, $I_t(x', y') = I_{t,x}(x')\, I_{t,y}(y')$. If (x, y) is divided into $N \times$ grid of M: $x = x_j$, $y = y_i$, $i = 1, 2, \cdots, n$, $j = 1, 2, \cdots, m$, then one can obtain x_j' and y_i' by

$$\int_{x_1}^{x_j} I_{\text{in},x}(x)dx \int_{y_1}^{y_n} I_{\text{in},y}(y)dy = \int_{x_1'}^{x_j'} I_{t,x}\left(x'\right)dx' \int_{y_1'}^{y_n'} I_{t,y}\left(y'\right)dy', \quad (11)$$

$$\int_{x_1}^{x_m} I_{\text{in},x}(x)dx \int_{y_1}^{y_i} I_{\text{in},y}(y)dy = \int_{x_1'}^{x_m'} I_{t,x}\left(x'\right)dx' \int_{y_1'}^{y_i'} I_{t,y}\left(y'\right)dy'. \quad (12)$$

According to the above mapping relationship $x_j' = f(x_j)$ and $y_i' = f(y_i)$, one can obtain an initial vector of outgoing light as $\mathbf{O}_{i,j} = \text{Unit}(x_j' - x_j, y_i' - y_i, d)$, where the Unit symbol means to find the unit vector and d is the integral value of the data. If the incident ray vector is $\mathbf{I}_{i,J} = (0, 0_i, 1)$, then the normal vector can be calculated by

$$\left[1 + n^2 - 2n\left(\mathbf{O}_{i,j} \cdot \mathbf{I}_{i,j}\right)\right]^{1/2} \mathbf{N}_{i,j} = \mathbf{O}_{i,j} - n\mathbf{I}_{i,j}. \quad (13)$$

According to the normal vector distribution calculated by the above formula, the discrete data points of the free-form surface are obtained by the least square method. Then, the classical field tracing mode is used to simulate the detection illuminance. The waist radius of the incident beam is 2.5 mm, and twice the waist is adopted; that is, the beam energy within 10 mm in diameter is considered. The divergence half-angle of the linear distribution of the target is 0.5 degrees in the X direction and 10.3 arcseconds in the Y direction. The incident surface of the lens is a plane, and the exit surface is a free-form surface to be solved. Figure 7

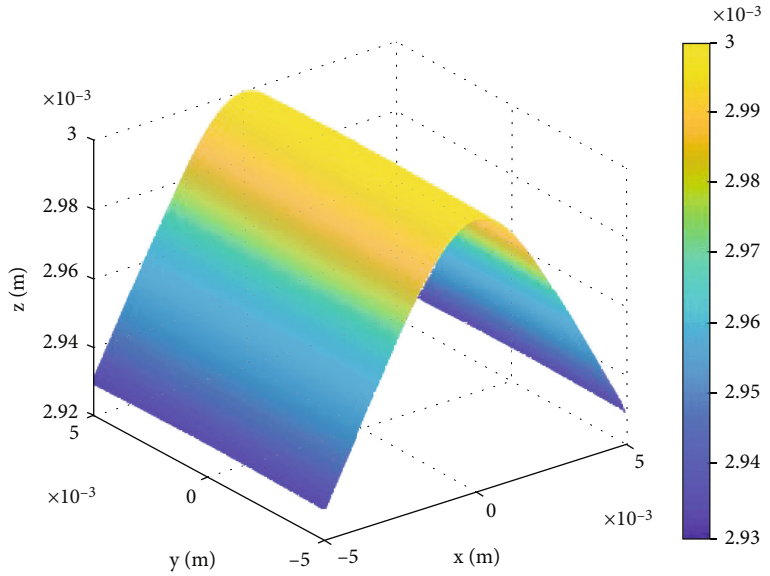

Figure 7: Optical free curved surface for laser transmitting system.

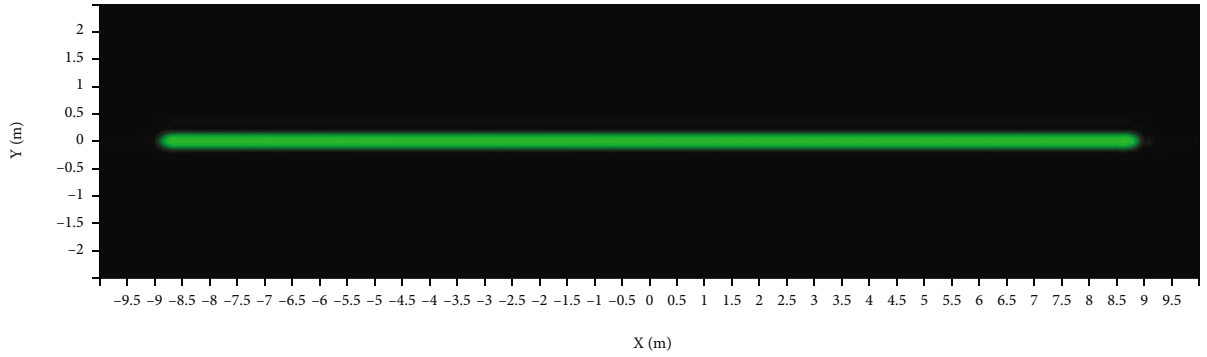

Figure 8: Illumination distribution on the position of $Z = 1$ km.

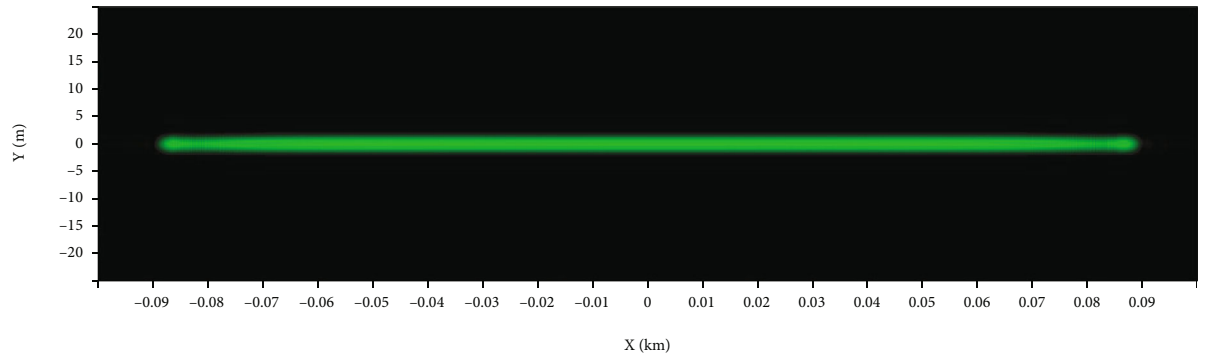

Figure 9: Illumination distribution on the position of $Z = 10$ km.

shows the calculated optical free-form surface shape, which is close to a cylindrical structure, and its vector height sag is 0.71 mm. The process of targeting from near to far is simulated. The object distance of the measured target includes 1 m, 10 m, 100 m, 1 km, 10 km, and 500 km. Figures 8–11 show the illuminance distribution at $z = 1$ km and $z = 500$ km. Through the simulation analysis, when the light source passes through the free-form surface lens, there is a process of convergence and divergence. When the object distance $z = 10$ m, the linear beam increases proportionally.

It can be seen from the statistical results of illuminance in Figure 11 that the beam intensity after free-form surface shaping starts to show an excellent linear distribution after traveling 10 m, and its distribution still has good uniformity

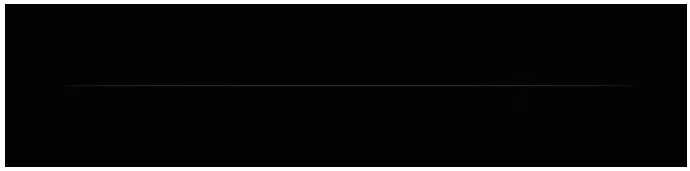

Figure 10: Illumination distribution on the position of $Z = 500$ km.

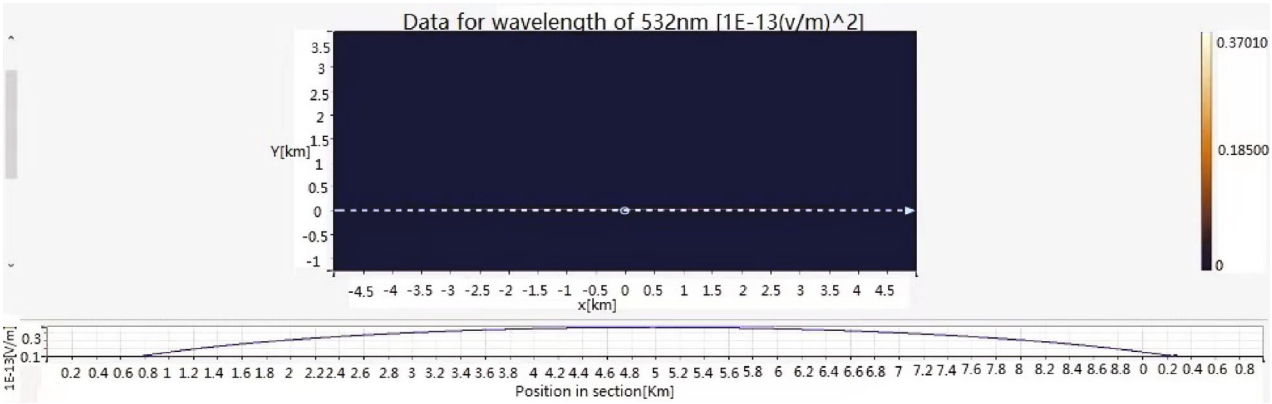

Figure 11: Laser illumination statistics on the position of $Z = 500$ km.

when the object distance reaches 500 km. This distribution is conducive to the full utilization of laser energy at the detection end, and loss reduces the laser's energy after ultra-long-distance propagation as much as possible.

The simulation shows that the dead time of the detector is linearly inversely proportional to the receiving aperture [22, 23]. Under the premise of ensuring the same signal contrast, the allowable receiving area can be increased by about 4~6 times compared with the single-pixel detector using the multielement detector. For different contrast and signal photon-counting events, the more detection counts, the greater the detection probability, and the higher the contrast, the earlier the detection probability reach the peak under the same signal photon-counting event [24, 25]. When the contrast is five and the signal photon count in the data frame is 35, the photon detection probability reaches the maximum, and the false alarm rate is the lowest. Therefore, to achieve high detection probability and minimum false alarm rate, the comprehensive influence of photon counting, dead time, and contrast needs to be considered in the design process. At the system level, according to the influence of detector dead time on ranging accuracy index, the detection probability and detection illuminance of single-photon LiDAR are simulated and analyzed, and the detection illuminance distribution of LiDAR under different object distances is obtained.

5. Conclusion

In this paper, the influence of the slow time of a single-photon detector on ranging accuracy, detection probability, and detection illumination in tandem single-photon LiDAR ranging is modeled and simulated. The influence relationship of detector dead time is established under different detection contrast. The simulation shows that by reasonably controlling the dead time and effective receiving aperture of the detector and using the free-form surface optical receiving system, the shaped beam intensity shows an excellent linear distribution after propagating a distance of 10 m. Its distribution still has good uniformity outside the object distance of 500 km, which proves the effectiveness and rationality of the simulation model of this method.

Data Availability

The data used to support the findings of this study are included within the article.

Conflicts of Interest

We declare that we have no conflict of interest.

References

[1] D. Renker and E. Lorenz, "Advances in solid state photon detectors," *Journal of Instrumentation*, vol. 4, no. 4, p. P04004, 2009.

[2] G. Q. Zhang, X. B. Hu, C. Z. Hu et al., "Demonstration of a silicon photomultiplier with bulk integrated quenching resistors on epitaxial silicon," *Nuclear Instruments and Methods in Physics Research Section A: Accelerators, Spectrometers, Detectors and Associated Equipment*, vol. 621, no. 1-3, pp. 116–120, 2010.

[3] K. Shi, C. Liu, Z. Sun, and X. Yue, "Coupled orbit-attitude dynamics and trajectory tracking control for spacecraft electromagnetic docking," *Applied Mathematical Modelling*, vol. 101, pp. 553–572, 2022.

[4] C. Liu, X. Yue, J. Zhang, and K. Shi, "Active disturbance rejection control for delayed electromagnetic docking of spacecraft

in elliptical orbits," *IEEE Transactions on Aerospace and Electronic Systems*, vol. 58, no. 3, pp. 2257–2268, 2022.

[5] K. Shi, C. Liu, J. D. Biggs, Z. Sun, and X. Yue, "Observer-based control for spacecraft electromagnetic docking," *Aerospace Science and Technology*, vol. 99, article 105759, 2020.

[6] C. Liu, G. Vukovich, Z. Sun, and K. Shi, "Observer-based fault-tolerant attitude control for spacecraft with input delay," *Journal of Guidance, Control, and Dynamics*, vol. 41, no. 9, pp. 2041–2053, 2018.

[7] X. Shao, Q. Hu, Z. H. Zhu, and Y. Zhang, "Fault-tolerant reduced-attitude control for spacecraft constrained boresight reorientation," *Journal of Guidance, Control, and Dynamics*, pp. 1–15, 2022.

[8] X. Shao and Q. Hu, "Immersion and invariance adaptive pose control for spacecraft proximity operations under kinematic and dynamic constraints," *IEEE Transactions on Aerospace and Electronic Systems*, vol. 57, no. 4, pp. 2183–2200, 2021.

[9] C. Liu, X. Yue, and Z. Yang, "Are nonfragile controllers always better than fragile controllers in attitude control performance of post-capture flexible spacecraft?," *Aerospace Science and Technology*, vol. 118, article 107053, 2021.

[10] J. M. Stoker, Q. A. Abdullah, A. Nayegandhi, and J. Winehouse, "Evaluation of single photon and Geiger mode LiDAR for the 3D elevation program," *Remote Sensing*, vol. 8, no. 9, p. 767, 2016.

[11] A. Swatantran, H. Tang, T. Barrett, P. DeCola, and R. Dubayah, "Rapid, high-resolution forest structure and terrain mapping over large areas using single photon lidar," *Scientific Reports*, vol. 6, no. 1, pp. 1–12, 2016.

[12] K. Y. Shrestha, W. E. Carter, K. C. Slatton, and T. K. Cossio, "Shallow bathymetric mapping via multistop single photoelectron sensitivity laser ranging," *IEEE Transactions on Geoscience and Remote Sensing*, vol. 50, no. 11, pp. 4771–4790, 2012.

[13] N. A. Forfinski-Sarkozi and C. E. Parrish, "Analysis of MABEL bathymetry in Keweenaw Bay and implications for ICESat-2 ATLAS," *Remote Sensing*, vol. 8, no. 9, p. 772, 2016.

[14] B. Du, C. Pang, D. Wu et al., "High-speed photon-counting laser ranging for broad range of distances," *Scientific Reports*, vol. 8, no. 1, p. 4198, 2018.

[15] T. Cossio, K. C. Slatton, W. Carter, K. Shrestha, and D. Harding, "Predicting topographic and bathymetric measurement performance for low-SNR airborne lidar," *IEEE Transactions on Geoscience and Remote Sensing*, vol. 47, no. 7, pp. 2298–2315, 2009.

[16] L. Xue, D. Zhai, Y. Li et al., "Ranging capability analysis for laser ranging system using superconducting nanowire detectors," *Acta Optica Sinica*, vol. 36, no. 3, p. 0304001, 2016.

[17] Q. Li, J. Degnan, T. Barrett, and J. Shan, "First evaluation on single photon-sensitive lidar data," *Photogrammetric Engineering and Remote Sensing*, vol. 82, no. 7, pp. 455–463, 2016.

[18] C. Yao, W. Chen, and G. Zang, "Accurate measurement of sea surface in an airborne laser bathymetry," *Infrared and Laser Engineering*, vol. 32, no. 4, pp. 351–355, 2003.

[19] A. Axelsson, "Rapid topographic and bathymetric reconnaissance using airborne LiDAR," in *Proceedings Volume 7835, Electro-Optical Remote Sensing, Photonic Technologies, and Applications IV*, pp. 39–48, Toulouse, France, 2010.

[20] C. Liu, X. Yue, K. Shi, and Z. Sun, "Inertia-free attitude stabilization for flexible spacecraft with active vibration suppression," *International Journal of Robust and Nonlinear Control*, vol. 29, no. 18, pp. 6311–6336, 2019.

[21] C. Liu, K. Shi, X. Yue, and Z. Sun, "Inertia-free saturated output feedback attitude stabilization for uncertain spacecraft," *International Journal of Robust and Nonlinear Control*, vol. 30, no. 13, pp. 5101–5121, 2020.

[22] M. Ghioni, A. Gulinatti, I. Rech, F. Zappa, and S. Cova, "Progress in silicon single-photon avalanche diodes," *IEEE Journal of Selected Topics in Quantum Electronics*, vol. 13, no. 4, pp. 852–862, 2007.

[23] L. Zheng-Ping, X. Huang, Y. Cao et al., "Single-photon computational 3D imaging at 45 km," *Photonics Research*, vol. 8, no. 9, pp. 1532–1540, 2020.

[24] T. Yin, N. Lauret, and J. P. Gastellu-Etchegorry, "Simulation of satellite, airborne and terrestrial LIDAR with DART (II): ALS and TLS multi-pulse acquisitions, photon counting, and solar noise," *Remote Sensing of Environment*, vol. 184, pp. 454–468, 2016.

[25] J. J. Degnan, "Scanning, multibeam, single photon Lidars for rapid, large scale, high resolution, topographic and bathymetric mapping," *Remote Sensing*, vol. 8, no. 11, p. 958, 2016.

Hindawi
International Journal of Aerospace Engineering
Volume 2022, Article ID 4650730, 16 pages
https://doi.org/10.1155/2022/4650730

Research Article

Maneuver Strategy for Active Spacecraft to Avoid Space Debris and Return to the Original Orbit

Qun Fang, Zhen Zhang, Haodong Meng, Xiaolong Wang, and Xiuwei Zhang

National Key Laboratory of Aerospace Flight Dynamics Technology, Northwestern Polytechnical University, Xi'an 710072, China

Correspondence should be addressed to Zhen Zhang; zhangzhennwpu@163.com

Received 5 January 2022; Accepted 24 March 2022; Published 13 April 2022

Academic Editor: Giovanni Palmerini

Copyright © 2022 Qun Fang et al. This is an open access article distributed under the Creative Commons Attribution License, which permits unrestricted use, distribution, and reproduction in any medium, provided the original work is properly cited.

During normal operation of the on-orbit spacecraft, if some satellite in a nearby orbit suddenly breaks apart, its debris will threat the safe operation of the on-orbit spacecraft. Therefore, it is necessary to study the active spacecraft's avoidance of the space debris group and returning to the original orbit. In this way, the safe operation of on-orbit spacecraft will be guaranteed. However, as the geometric structure of the space debris group is constantly changing, it is hard to accurately demonstrate the changing shape of the debris group, let alone determine the unreachable domain. Traditional obstacle avoidance problems involve low speed of the vehicle; so, the application of artificial potential field and particle swarm algorithms is suitable for such problems. However, these two methods are not applicable to the maneuver strategy of spacecraft with high initial velocity. Therefore, to help spacecraft avoid the space debris group, a new method is required. This paper has established a simplified model to simulate the unreachable domain of the space debris group. It has modified the artificial potential field (APF) method and particle swarm optimization algorithm, with an aim to help spacecraft avoid the space debris group and return to the original orbit. Based on the method, the paper has proposed a three-stage maneuver strategy for the spacecraft to avoid the debris. To show the effectiveness of the method, this paper has simulated an on-orbit spacecraft's avoidance of the space debris group nearby and returning to its original orbit. Through simulation, the feasibility of the maneuver strategy for spacecraft in the geosynchronous orbit is evaluated. The simulation results show that the method proposed in this paper can effectively accomplish the task.

1. Introduction

With the rapid development of the space technology, the number of space orbit debris keeps increasing. According to the United States Space Surveillance Network, by the end of December 2021, there were more than 36,500 space debris with diameters larger than 10 cm littering space. More than 630 dangerous events have happened due to collisions or breakups of space debris [1]. As space debris fragments are travelling at fast speed, once they crash into the on-orbit spacecraft, the spacecraft will be severely damaged or even shattered. In history, many space collisions happened. For example, in 1991, Russian satellite COSMOS1934 collided with debris No. 13475 [2]; in 1996, the French spacecraft "Cerise" and space debris No. 18208 hit each other [3]; in 2005, THORBURNER 2A rocket collided with debris No. 26207 [3], and in 2009, two communications satellites—the commercial Iridium 33 and the Russian military Cosmos 2251—accidentally collided [4]. Every high-speed collision will scatter a larger number of smaller debris and form a vicious cycle. For example, the collision of Iridium 33 and Cosmos 2251 in 2009 generated 2,201 pieces of debris in total [5]. The collision between space objects not only poses a huge threat to the on-orbit spacecraft but also becomes the biggest contributor to the increasing of space debris [6, 7].

With the development of space technology, the number of spacecrafts increases gradually. When the on-orbit spacecraft is working, if there is a sudden breakup of satellite near the orbit, a debris group will be produced. The debris group will severely threat the safe operation of on-orbit spacecraft. To reduce the threat caused by the space debris from satellite breakup, we need to study the maneuver strategy for the on-orbit spacecraft to avoid the space debris group and return

to its original orbit. This is an important precondition for the safe operation of the spacecraft. Space debris and debris group pose different threats to spacecraft in orbit. The problem of active spacecraft evading space debris is a point-to-point problem. Only a fixed safety threshold needs to be considered when the spacecraft avoids space debris. In contrast, the space debris group spreads over time; so, it is necessary to consider the constantly changing geometry of the space debris group to avoid them. Currently, many scholars have studied the spacecraft avoidance strategy. Russell focused on calculating the collision probability among space objects, and he proposed to replace sphere colliders with cylindrical colliders [8]. After considering the general thrust and the control and maintenance of the spacecraft's orbit and location, Chan proposed a maneuvering speed expression. His expression was based on the collision probability [9]. Alfano and Mueller proposed other appropriate strategies to solve the collision avoidance problem [10, 11]. Alfano analyzed the instantaneous maneuvering speed [10] while Mueller et al. used the standard form of optimal control to express the avoidance problem [11]. In Mueller's study, the problem was discretized and transformed from a control problem into a nonlinear planning problem. Mueller et al. proposed a method to control the spacecraft and avoid on-orbit collision [12]. This method is applied to both situations when the two objects had a high relative velocity or a low one. It has a certain robustness. Besides, this method would prevent a second collision for a long time after the first maneuvering. Graziano et al. thoroughly introduced the basic principle for detecting and estimating the risks of satellite collision. He analyzed the operating procedure of collision prevention and summarized the rules for the maneuver strategy of avoidance [13]. Kelly and Piciotto adopted nonlinear optimization technology to study the optimal collision avoidance maneuvering calculation [14]. Based on the state-transition matrix, Gonzalo and Colombo designed an orbit maneuver strategy under the pulse thrust and analyzed its effectiveness [15]. They also analyzed the orbit maneuvering design under constant thrust provided along the velocity tangential direction [16] and added the results into a computer program to calculate the orbit maneuver [17]. Zhang et al. proposed an efficient method to calculate the diffusion law of space debris groups over time [18]. Dharmarajan et al. studied the method of satellite formation to avoid space debris. He proposed that the time of applying correction should be determined based on the capability of the satellite performing the maneuver. Moreover, he offered a method to solve eigenvalues in the optimization of maximum range and minimum velocity [19]. Most scholars mainly concentrated on how spacecraft can avoid space debris or regular space objects, but few of them studied how spacecraft can avoid the space debris group from the breakup of satellites in the neighboring orbit.

This paper focuses on the maneuver strategy of spacecraft to avoid the space debris group, which are generated by the breakup of objects in neighboring orbit, and then return to its original orbit. It proposes a simplified method of the unreachable domain for the space debris group. Through the modification of artificial potential field (APF) and particle swarm optimization (PSO) algorithms, the spacecraft will complete the maneuvering process through three stages: the stage of avoidance, the stage of returning from a distant proximity, and the stage of returning from a close proximity. Next, the paper verifies the effectiveness of this method through a simulation experiment.

2. Dynamic Modeling

2.1. Selection of the Coordinate System. To accurately demonstrate the orbital motion of the active spacecraft and the space debris group, the earth-centered inertial (ECI) coordinate system $OXYZ$ is defined as can be shown in Figure 1: the coordinate system has its origin O at the center of the Earth, the OX axis is aligned with the mean equinox at epoch J2000, the OZ axis is aligned with the Earth's North Pole, the OY axis is established by the right-hand rule, and P is an on-orbit spacecraft.

To describe the orbital motion of an active spacecraft during the close return stage (Figure 1), the CW coordinate system $O'X'Y'Z'$ is defined (Figure 2): the coordinate system has its origin O' at the center of the mass of the target point, the $O'X'$ axis is aligned with the center of mass of the target along the center of the earth, the $O'Y'$ axis is aligned with the direction of motion of the target point, which is in the orbital plane of the target point and perpendicular to the $O'X'$ axis, and the $O'Z'$ axis is established by the right-hand rule.

2.2. The Dynamic Equation of the Active Spacecraft and the Space Debris Group. If the spacecraft can complete its task within a short period, it is reasonable to suppose that the influence of the perturbation term can be ignored. As the spacecraft needs to urgently avoid a close debris group, it is assumed that the spacecraft and space debris group are not affected by perturbation forces during their motion.

The ECI system is selected to illustrate the orbital motion of the active spacecraft and space debris. The dynamic equation is

$$\ddot{\mathbf{r}} = -\frac{\mu}{r^3}\mathbf{r}, \tag{1}$$

where $\ddot{\mathbf{r}}$ is the acceleration vector of the space goal, μ denotes the geocentric gravitational constant, r means the geocentric distance of the space goal, and $\mathbf{r}$ represents the distance vector from the space goal to the center of Earth.

2.3. Discretization of the Relative Dynamic Equation. When the spacecraft is relatively close to the goal, the CW equation of the goal relative to the spacecraft is usually established under the CW coordinate system.

$$\begin{cases} \ddot{x} - 2n\dot{y} - 3n^2 x = f_x, \\ \ddot{y} + 2n\dot{x} = f_y, \\ \ddot{z} + n^2 z = f_z, \end{cases} \tag{2}$$

where $\ddot{x}$, $\ddot{y}$, and $\ddot{z}$ are the relative accelerations of the

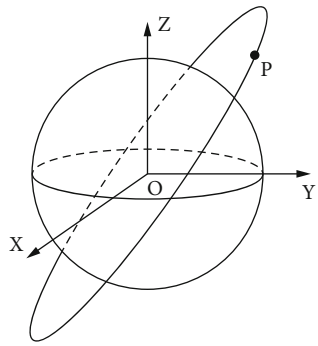

Figure 1: Diagram of the Earth-Centered Inertial (ECI) coordinate system.

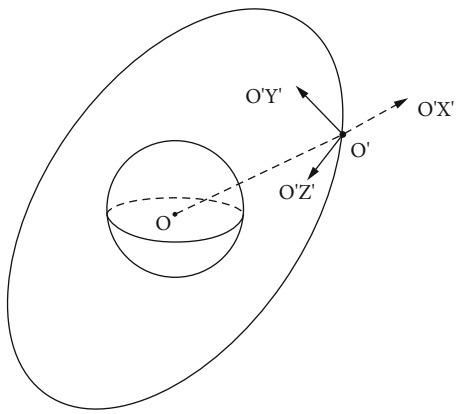

Figure 2: Diagram of the CW coordinate system.

spacecraft to the goal in three directions of the CW coordinate system; $\dot{x}$ and $\dot{y}$ are the relative velocities of the spacecraft to the goal; x and z are the relative location of the spacecraft to the goal in the directions of $O'X'$ and $O'Z'$ under the CW coordinate system; f_x, f_y, and f_z are the thrust accelerations of the spacecraft relative to the goal in the three directions of the CW coordinate system; and n is the mean angular velocity.

$$n = \sqrt{\frac{\mu}{r_0^3}}, \tag{3}$$

where μ denotes the geocentric gravitational constant, and r_0 is the goal's geocentric distance.

Based on linear systems theory, formula (2) is discretized [20], and the state-transition matrix of the spacecraft is obtained.

$$\mathbf{X}(t) = \mathbf{\Gamma}(t - t_0)\mathbf{X}(t_0) + \int_{t_0}^{t} \mathbf{\Gamma}(t - \tau)\mathbf{B}\mathbf{u}(\tau)d\tau, \tag{4}$$

where

$$\mathbf{\Gamma}(t - t_0) = \mathbf{\Gamma}(\Delta t) = \begin{bmatrix} \mathbf{\Gamma}_{rr}(\Delta t) & \mathbf{\Gamma}_{rv}(\Delta t) \\ \mathbf{\Gamma}_{vr}(\Delta t) & \mathbf{\Gamma}_{vv}(\Delta t) \end{bmatrix}, \Delta t = t - t_0, \tag{5}$$

$$\mathbf{\Gamma}_{rr}(\Delta t) = \begin{bmatrix} 4 - 3\cos n\Delta t & 0 & 0 \\ 6(\sin nt - n\Delta t) & 1 & 0 \\ 0 & 0 & \cos n\Delta t \end{bmatrix}, \tag{6}$$

$$\mathbf{\Gamma}_{rv}(\Delta t) = \begin{bmatrix} \frac{1}{n}\sin n\Delta t & \frac{2}{n}(1 - \cos n\Delta t) & 0 \\ \frac{2}{n}(\cos n\Delta t - 1) & \frac{1}{n}(4\sin n\Delta t - 3n\Delta t) & 0 \\ 0 & 0 & \frac{1}{n}\sin n\Delta t \end{bmatrix}, \tag{7}$$

$$\mathbf{\Gamma}_{vr}(\Delta t) = \begin{bmatrix} 3n\sin n\Delta t & 0 & 0 \\ 6n(\cos n\Delta t - 1) & 0 & 0 \\ 0 & 0 & -n\sin n\Delta t \end{bmatrix}, \tag{8}$$

$$\mathbf{\Gamma}_{vv}(\Delta t) = \begin{bmatrix} \cos n\Delta t & 2\sin n\Delta t & 0 \\ -2n\sin n\Delta t & 4\cos n\Delta t - 3 & 0 \\ 0 & 0 & \cos n\Delta t \end{bmatrix}. \tag{9}$$

Considering that when the spacecraft returns to the goal, it will control the velocity impulse for many times, and this paper discretized the system's continuous time into T time intervals. The formula (4) can be shown as

$$\mathbf{X}_{k+1} = \mathbf{\Gamma}_k\mathbf{X}_k + \mathbf{G}_k\mathbf{u}_k, \tag{10}$$

where k indicates the k-$^{\text{th}}$ interval, $\mathbf{u}_k = [u_{kx}, u_{ky}, u_{kz}]^T$ denotes the accelerations generated by the spacecraft in three directions under the CW coordinate system, and $\mathbf{\Gamma}_k$ and $\mathbf{G}_k$ are the discretized state-space matrix. Their definitions are as follows:

$$\begin{aligned} &\mathbf{\Gamma}_k = \mathbf{\Gamma}(T) \triangleq \text{const}, \\ &\mathbf{G}_k = \mathbf{G}(T) = \int_0^T \mathbf{\Gamma}(\tau)\mathbf{B}d\tau \triangleq \text{const}. \end{aligned} \tag{11}$$

As the time interval T is fixed, when the spacecraft is maneuvered for the N-$^{\text{th}}$ times, the state quantity of the spacecraft is

$$\mathbf{X}_N = \mathbf{\Gamma}^N\mathbf{X}_0 + \widetilde{\mathbf{\Gamma}}\tilde{\mathbf{u}}, \tag{12}$$

where

$$\begin{aligned} &\widetilde{\mathbf{\Gamma}} = \left[\mathbf{\Gamma}^{N-1}\mathbf{G}, \mathbf{\Gamma}^{N-2}\mathbf{G}, \cdots, \mathbf{G}\right], \\ &\tilde{\mathbf{u}} = \left[\mathbf{u}_0, \mathbf{u}_1, \cdots, \mathbf{u}_{N-1}\right]^T. \end{aligned} \tag{13}$$

Formula (12) is the dynamic model of the relative motion after the discretization of the average time. Using formula (12), we can obtain the motion state of the spacecraft relative to the goal at the time of $t = t_0 + \text{NT}$ under the influence of the velocity impulse. Likewise, if the spacecraft wants to reach a certain state X_{t+T} at the time of $t +$

T, formula (13) can also generate the amplitude and direction of the velocity impulse $\boldsymbol{u}_t$ that is exerted by the spacecraft at the time of t.

3. Generative Model of the Space Debris Group

To simulate the space debris group in the orbit near the active spacecraft, this paper adopts the model of NASA EVOLVE 4.0 [21] as an analog simulator to get information about the space debris fragments, including lengths, areas, mass, and speed increments.

The breakup model of NASA EVOLVE 4.0 can be divided into two parts: the explosion breakup and the collision breakup. As they will not affect the application of the proposed algorithm of rapid orbital evolution, the two parts will be considered as one natural breakup, i.e., explosion breakup, without a loss of generality. Formula (14) calculates the size of every debris fragment:

$$\begin{cases} N(L_c \geq L_i) = \tau \cdot 6 \cdot L_i^{-1.6}, i = 1, 2 \cdots n, \\ N(L_c = L_i) = N(L_c \geq L_i) - N(L_c \geq L_{i+1}), \end{cases} \tag{14}$$

where τ is the constant coefficient, 4.5 is the usually adopted value, L_c is the characteristic length, which is derived by taking the average number of the debris lengths in three directions, namely, $L_c = (l_x + l_y + l_z)/3$, and $N(L_c \geq L_i)$ indicates the number of debris fragments with characteristic length longer than L_i. The shorter the interval of L_i is, the closer it is to the reality.

Using the lengths of space debris, we can further determine the area-to-mass ratio (AMR) of each debris with binormal distribution (15):

$$\begin{cases} \chi = \alpha N(\mu_1, \sigma_1) + (1 - \alpha) N(\mu_2, \sigma_2), \\ N(\mu_i, \sigma_i) = \dfrac{1}{\sqrt{2\pi}\sigma_i} e^{-\frac{(\chi - \mu_i)^2}{2\sigma_i^2}}, i = 1, 2, \end{cases} \tag{15}$$

where α is the weight coefficient, and μ_i and σ_i are the mean and variance of the normal distribution, respectively. The characteristic lengths of the three parameters are obtained through the logarithm of the characteristic lengths $\log_{10}(L_c)$ [19], and χ denotes the logarithm of the AMR with $\chi \triangleq \log_{10}(A/M)$.

The mass of space debris is obtained by formula (16).

$$M = \frac{A_x}{\eta}, \tag{16}$$

where A_x is the average cross-sectional area. The average cross-sectional area of each piece of the space debris is determined by its characteristic length [19] and acquired through formula (17): $\eta = 10^{\chi}$.

$$A_x = \begin{cases} 0.540424 L_c^{\,2}, & L_c < 0.00167m, \\ 0.556945 L_c^{\,2.0047077}, & L_c \geq 0.00167m. \end{cases} \tag{17}$$

After the explosion and breakup, space debris will pick up a speed increment, which is obtained by formula (9):

$$\Upsilon = \frac{1}{\sqrt{2\pi}\sigma} e^{-\frac{(\chi - \mu)^2}{2\sigma^2}}, \tag{18}$$

where Υ is the logarithm of the speed increment, i.e., $\Upsilon = \log_{10}(\Delta v)$; μ is determined by χ, the logarithm of the AMR, i.e., $\mu = 0.2\chi + 1.85$; and σ is the constant of 0.4. The direction of the speed increment satisfies three dimensional random uniform distribution [22].

4. Maneuver Strategy of the Active Spacecraft's Avoidance and Return

This section will establish a simplified model to simulate the unreachable domain of the space debris group. It will introduce the spacecraft maneuver strategy at the stage of avoidance, the stage of returning from a distant proximity, and the stage of returning from a proximity.

4.1. Modeling of the Unreachable Domain. For the space debris group, the state of every space debris $\boldsymbol{\Omega}_i(t)$ can be simulated with a four-dimensional vector:

$$\boldsymbol{\Omega}_i(t) = f(x_i, y_i, z_i, t) \subset \mathbb{R}, \tag{19}$$

where $\boldsymbol{\Omega}_i(t)$ can be obtained through numerical integration of formula (1). $\boldsymbol{\Omega}_i(t)$ represents the state of the i^{th} space debris at the time of t; x_i, y_i, and z_i indicate the components of location vectors of the i^{th} space debris during its entire motion at the ECI coordinate system, respectively, and $\mathbb{R}$ shows the state space consisting of all the space debris states during the entire motion.

The orbital plane of the on-orbit spacecraft is defined as space $\mathbb{Z}$. Thus, the intersection of each space debris $\boldsymbol{\Omega}_i$ and the orbital plane is

$$\mathbf{Q}_i = \boldsymbol{\Omega}_i \cap \mathbb{Z}, \tag{20}$$

where $\mathbf{Q}_i = \{x_i, y_i, z_i\}$ indicates the intersection of the i^{th} space debris and the spacecraft's orbital plane, and x_i, y_i, and z_i are the three coordinates of the intersection.

The problem of active spacecraft's avoidance of the space debris group is a four-dimensional problem; so, the active spacecraft needs to stay away from the space debris $\boldsymbol{\Omega}_i$ at the time of t. However, in reality, the calculation costs are high, as there are a large number of space debris in a debris group, which are hard to be analyzed one by one. Besides, the geometry of the space debris group will considerably change with the altering initial value. It is difficult to simulate using a unified mathematic rule. Therefore, dimension reduction is used in the model to present the threat of the space debris group. In other words, the two-dimensional space avoidance problem is transformed into an avoidance problem on a four-dimensional plane.

According to formula (20), if $\mathbf{Q}_i = \boldsymbol{\Omega}_i \cap \mathbb{Z} = \varnothing$, there is no threat from the space debris to collide with the spacecraft;

if $\mathbf{Q}_i = \mathbf{\Omega}_i \cap \mathbb{Z} \neq \varnothing$, then $\mathbf{Q}_i$ serves as the dangerous point for further discussion of modeling the unreachable domain.

The set of coordinates for all dangerous points can be expressed as

$$\mathbb{Z}_{s_d} = \{\mathbf{Q}_1, \mathbf{Q}_2, \cdots, \mathbf{Q}_i, \cdots, \mathbf{Q}_N\} = \mathbb{R} \cap \mathbb{Z}. \tag{21}$$

It should be noted that $\mathbb{Z}_{s_d}$ shows the set space of all the dangerous points. All the points inside the space are on the orbital plane $\mathbb{Z}$:

$$\mathbb{Z}_{s_d} \subset \mathbb{Z}.. \tag{22}$$

A circular envelope is used to encompass all the dangerous points $\mathbb{Z}_{s_d}$ to form an unreachable domain $\mathbb{Z}_{ud}$. Thus, this unreachable domain is a circular no-fly zone on the orbital plane $\mathbb{Z}$. The centre of the circle $\mathbf{Q}_{\text{ud}}$ is as follows:

$$\mathbf{Q}_{\text{ud}} = \frac{\sum_{i=1}^{N} \mathbf{Q}_i}{N}. \tag{23}$$

As for the $i_^{\text{th}}$ dangerous point $\mathbf{Q}_i$, which is the distance from $\mathbf{Q}_i$ to the center of the unreachable circle, $\mathbf{Q}_{\text{ud}}$ can be derived as follows:

$$r_i = \sqrt{(x_i - x_{ud})^2 + (y_i - y_{ud})^2 + (z_i - z_{ud})^2}. \tag{24}$$

Thus, the radius of the unreachable domain is

$$r_{ud} = \max\{r_1, r_2, \cdots, r_i, \cdots, r_N\}. \tag{25}$$

Thus, the no-fly zone of the space debris group on the spacecraft's orbital plane is obtained. If the active spacecraft can avoid the unreachable domain, of which the center of the circle is $\mathbf{Q}_{ud}$ and the radius is r_{ud}, the danger from the space debris group can be avoided.

4.2. The Stages of the Spacecraft's Task. Based on the requirement of the problem, the task of the spacecraft can be divided into the stage of avoidance, the stage of returning from a distant proximity, and the stage of returning from a close distance. To enable the spacecraft's avoidance of the space debris group, an unreachable domain is established as the no-fly zone in Section 3.1; to enable the spacecraft's return to the original orbit, the goal is that the spacecraft should move back to the initial orbit. In other words, reaching back to the location and state of the spacecraft when it has not maneuvered is the goal.

Suppose that the distance from the spacecraft to the no-fly zone at the time of t_f is $\|d_{rep}\|_f$, the distance at the time of t_{f+1} is $\|d_{rep}\|_{f+1}$. If $\|d_{rep}\|_f > \|d_{rep}\|_{f+1}$, then the spacecraft should be considered as moving closer to the no-fly zone. At this time, the task of the spacecraft is to avoid the no-fly zone, and this period can be regarded as the stage of avoidance; conversely, if $\|d_{rep}\|_f \leq \|d_{rep}\|_{f+1}$, the spacecraft is considered to be flying away from the no-fly zone, and this period can be regarded as the stage of returning from a distant proximity.

Suppose that the distance from the spacecraft to the goal at the time of t_k is $\|d_{att}\|_k$, and at the time of t_{k+1}, its distance to the goal becomes $\|d_{att}\|_{k+1}$. If $\|d_{att}\|_k > \|d_{att}\|_{k+1}$, the spacecraft is considered to be closer to the goal. This is when the spacecraft is at the stage of returning from a distant proximity; conversely, if $\|d_{att}\|_k \leq \|d_{att}\|_{k+1}$, the adopted method fails, and the spacecraft enters the stage of returning from a close proximity.

4.3. The Maneuver Strategy of the Spacecraft at the Stage of Avoidance. At the stage of avoidance, an artificial repulsive potential function is adopted to analyze the maneuver strategy for active spacecraft to avoid the space debris group. However, traditional repulsive potential functions are designed to solve problems such as the motion of robots with relatively small initial velocities or the rendezvous and docking of spacecrafts with a small relative velocity. For an active spacecraft to avoid the space debris group, there are some difficulties that have never occurred in traditional scenarios.

The spacecraft itself is running at a fast speed and has a relatively high inertia, and the artificial repulsive potential field is only effective when the two objects are close to each other. Thus, if the spacecraft only receives notable impact from the repulsive potential field when it is close to the no-fly zone, it needs a thrust higher than its upper limit to overcome its inertia and avoid the no-fly zone.

To solve these problems, the artificial potential field function needs to be modified. First, the distance values in the traditional repulsive potential are mapped to minimize the impact of the distance on the repulsive force; second, in contrast to the traditional repulsive potential field, the new method calculates the total force (thrust) instead of the repulsive potential field; third, the thrusts of the spacecraft at very moment are divided into the spacecraft velocity in the normal line direction [16].

To help the spacecraft stay away the no-fly zone, an artificial repulsive force field is established. Its repulsive potential function $U_{\text{rep}}(q)$ to the spacecraft is

$$U_{\text{rep}}(q) = \begin{cases} \dfrac{2}{5} \cdot k_{\text{rep}} \cdot \left(\dfrac{1}{q(\|d_{\text{rep}}\|)}\right)^{2.5}, & \|d_{\text{rep}}\| \leq d_0, \\ 0, & \|d_{\text{rep}}\| > d_0, \end{cases} \tag{26}$$

where k_{rep} is the gain coefficient, and $\|d_{\text{rep}}\|$ indicates the Euclidean distance from the active spacecraft to the no-fly zone. The specific definition is shown in formula (27), and $q(\|d_{\text{rep}}\|)$ denotes the mapping of the distance $\|d_{\text{rep}}\|$ within the interval of $[1, 2]$. The detailed definition is in formula (28), and d_0 is the influence distance from the no-fly zone's repulsive force field to the active spacecraft. If the distance between the spacecraft and the no-fly zone is smaller than this value, namely, $\|d_{\text{rep}}\| \leq d_0$, the spacecraft will be affected

by the repulsive force. Conversely, the spacecraft will not be affected by the repulsive force.

$$\left\|d_{\text{rep}}\right\| = \left\| \sqrt{(x - x_{\text{ud}})^2 + (y - y_{\text{ud}})^2 + (z - z_{\text{ud}})^2} - r_{\text{ud}} \right\|, \tag{27}$$

where x, y, and z are spacecraft's location components under the three axes of the ECI system; x_{ud}, y_{ud}, and z_{ud} indicate the coordinates of the center of the no-fly zone under the three axes of the ECI system; and r_{ud} represents the radius of the no-fly zone.

$$q\left(\left\|d_{\text{rep}}\right\|\right) = \frac{\left\|d_{\text{rep}}\right\|}{d_0} + 1. \tag{28}$$

Due to the special condition of the spacecraft's motion, when it is close to the no-fly zone, it is not able to maneuver and avoid the zone. Therefore, exerting distance from the repulsive force field needs to be projected to increase the influence of the field on the spacecraft when it enters the range of the repulsive force field.

The negative gradient of the repulsive potential field is the repulsive force received by the active spacecraft, namely,

$$\begin{aligned} F_{\text{rep}}(q) &= -\nabla U_{\text{rep}}(q) = -\frac{\partial U_{\text{rep}}(q)}{\partial q} \\ &= \begin{cases} k_{\text{rep}} \cdot \left(\dfrac{1}{q\left(\left\|d_{\text{rep}}\right\|\right)}\right)^{3.5}, & \left\|d_{\text{rep}}\right\| \le d_0 \\ 0, & \left\|d_{\text{rep}}\right\| > d_0 \end{cases}. \end{aligned} \tag{29}$$

Particularly, in formula (29), as $q(\|d_{\text{rep}}\|) \subset [1, 2]$, we get $(1/q(\|d_{\text{rep}}\|))^{3.5} \le 1$; so, the gain coefficient of repulsive potential field k_{rep} can obtain the upper limit of the thrust from the spacecraft. In this way, the thrust of the spacecraft will be less than its upper limit.

For further description, we define two concepts. At time t_0, if the spacecraft is not maneuvering, the geocentric distance of spacecraft at the next moment t_1 is D_n. If the spacecraft maneuvers, the geocentric distance of spacecraft at the next moment t_1 is D_m. If D_m is longer than D_n, e the altered orbit of spacecraft at time t_0 is defined as the ascending orbit. If D_m is shorter than D_n, the altered orbit of spacecraft at time t_0 is defined as descending orbit.

After the thrust is derived by formula (29), the direction of the thrust's distribution is to be determined. As can be shown in Figure 3, when the center P of the unreachable domain is located at the original orbit (the initial orbit), where the spacecraft has not maneuvered to change orbit, the altered orbit of spacecraft should be the descending orbit (orbit 1); when the center P of the unreachable domain is inside the initial orbit (orbit 2), the altered orbit of spacecraft should be the ascending orbit. Next, the distribution direction of the thrust is to be determined based on whether the

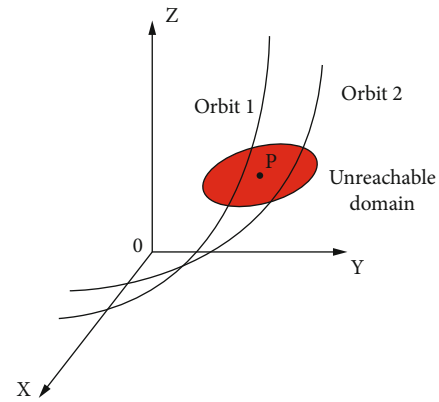

Figure 3: Illustration of thrust distribution.

altered orbit of spacecraft is the ascending or descending orbit.

Furthermore, the distribution of the thrust is illustrated in detail.

Three nonlinear points on the orbital plane of the spacecraft are obtained. They are $P_{sc1}(x_{sc1}, y_{sc1}, z_{sc1})$, $P_{sc2}(x_{sc2}, y_{sc2}, z_{sc2})$, and $P_{sc3}(x_{sc3}, y_{sc3}, z_{sc3})$, respectively. The normal vector of the spacecraft is

$$\overrightarrow{n_{sc}} = (\alpha_n, \beta_n, \gamma_n) = \overrightarrow{P_{sc1}P_{sc2}} \times \overrightarrow{P_{sc1}P_{sc3}}. \tag{30}$$

The velocity vector of the active spacecraft at a certain time is $\overrightarrow{v_{sc}} = (\alpha_v, \beta_v, \gamma_v)$. It is assumed that the direction of the exerted thrust is $\overrightarrow{F'_{rep}} = (\alpha'_{rep}, \beta'_{rep}, \gamma'_{rep})$. The thrust direction at this moment and the velocity vector $\overrightarrow{v_{sc}}$ are perpendicular to the normal vector $\overrightarrow{n_{sc}}$ of the orbital plane. Suppose that $\gamma'_{rep} = 1$, then the dot product of $\overrightarrow{v_{sc}}$ and $\overrightarrow{n_{sc}}$ with $\overrightarrow{F'_{rep}}$ is

$$\begin{cases} \alpha'_{\text{rep}} = \dfrac{\beta_v \cdot (\gamma_v - \alpha_v \cdot \gamma_n)}{\alpha_v \cdot (\alpha_v \cdot \beta_n - \beta_v)} - \dfrac{\gamma_v}{\alpha_v}, \\ \beta'_{\text{rep}} = \dfrac{\gamma_v - \alpha_v \cdot \gamma_n}{\alpha_v \cdot \beta_n - \beta_v}. \end{cases} \tag{31}$$

Formula (31) is further processed by normalizing the thrust direction vector $\overrightarrow{F'_{\text{rep}}} = (\alpha'_{\text{rep}}, \beta'_{\text{rep}}, \gamma'_{\text{rep}})$. The unit vector of the thrust direction $\overrightarrow{F_{\text{rep}}} = k_{\text{Frep}} \cdot (\alpha_{\text{rep}}, \beta_{\text{rep}}, \gamma_{\text{rep}})$ is

$$\begin{cases} \alpha_{\text{rep}} = \dfrac{\alpha'_{\text{rep}}}{\sqrt{\left(\alpha'_{\text{rep}}\right)^2 + \left(\beta'_{\text{rep}}\right)^2 + \left(\gamma'_{\text{rep}}\right)^2}} = \dfrac{\alpha'_{\text{rep}}}{\sqrt{\left(\alpha'_{\text{rep}}\right)^2 + \left(\beta'_{\text{rep}}\right)^2 + 1}}, \\ \beta_{\text{rep}} = \dfrac{\beta'_{rep}}{\sqrt{\left(\alpha'_{\text{rep}}\right)^2 + \left(\beta'_{\text{rep}}\right)^2 + \left(\gamma'_{\text{rep}}\right)^2}} = \dfrac{\beta'_{\text{rep}}}{\sqrt{\left(\alpha'_{\text{rep}}\right)^2 + \left(\beta'_{\text{rep}}\right)^2 + 1}}, \\ \gamma_{\text{rep}} = \dfrac{\gamma'_{rep}}{\sqrt{\left(\alpha'_{\text{rep}}\right)^2 + \left(\beta'_{\text{rep}}\right)^2 + \left(\gamma'_{\text{rep}}\right)^2}} = \dfrac{1}{\sqrt{\left(\alpha'_{\text{rep}}\right)^2 + \left(\beta'_{\text{rep}}\right)^2 + 1}}. \end{cases} \tag{32}$$

In Equation (32), k_{Frep} is 1 or -1, representing two-unit vectors with different directions.

As shown in Figure 4, when the spacecraft moves to a random point S, the thrust calculated based on the repulsive potential function is either $\overrightarrow{F_1}$ or $\overrightarrow{F_2}$, determined by the value of k_{Frep}.

To further specify the thrust direction, take $k_{v2} > k_{v1} > 0$, and the coordinates of A is $(k_{v1}\alpha_v, k_{v1}\beta_v, k_{v1}\gamma_v)$ and B is $(k_{v2}\alpha_v, k_{v2}\beta_v, k_{v2}\gamma_v)$, while $k_{\text{Frep}} = 1$, the coordinates of point C is $(\alpha_{\text{rep}}, \beta_{\text{rep}}, \gamma_{\text{rep}})$.

To figure out whether the point C's relative position to the vector AB on the orbital plane, project the points A, B, and C onto the xoy plane of the ECI coordinate system. Upon the projection, the coordinates of points A, B, and C are

$$\begin{cases} A' = (k_{v1}\alpha_v, k_{v1}\beta_v), \\ B' = (k_{v2}\alpha_v, k_{v2}\beta_v), \\ C' = \left(\alpha_{\text{rep}}, \beta_{\text{rep}}\right). \end{cases} \tag{33}$$

Connecting $A', B',$ andC' on the plane in the sequence to form an area which is defined as

$$\begin{aligned} S\left(A', B', C'\right) = &\left(k_{v1}\alpha_v - \alpha_{\text{rep}}\right) \cdot \left(k_{v2}\beta_v - \beta_{\text{rep}}\right) \\ &- \left(k_{v1}\beta_v - \beta_{\text{rep}}\right) \cdot \left(k_{v2}\alpha_v - \alpha_{\text{rep}}\right). \end{aligned} \tag{34}$$

When A',-B', and -C' are connected in a counterclockwise order, $S(A', B', C')$ is positive. When A',-B', and -C' are connected in a clockwise order, $S(A', B', C')$ is negative. In other words, if the vector starts from A' and ends at B', then the C' is on the right side of the vector $A'B'$ when Equation (33) is greater than 0, and the thrust in this direction will push the altered orbit of spacecraft ascend. If the C' is on the left side of the vector $A'B'$ when Equation (34) is less than 0, the thrust in this direction will make the altered orbit of spacecraft descend.

In summary, when the spacecraft needs to avoid collision by ascending it orbit, if $k_{\text{Frep}} = 1$, the thrust makes the altered orbit of spacecraft ascend. Based on Equations (29)and (32), the thrust in the three directions of the spacecraft is

$$\begin{cases} F_x = \alpha_{\text{rep}} \cdot F_{\text{rep}}(q), \\ F_y = \beta_{\text{rep}} \cdot F_{\text{rep}}(q), \\ F_z = \gamma_{\text{rep}} \cdot F_{\text{rep}}(q), \end{cases} \tag{35}$$

and vice versa.

4.4. Analysis on the Maneuver Strategy of Spacecraft at the Stage of Returning from a Distant Proximity. To design the orbit of the spacecraft returning from a distant proximity with artificial gravitational potential function, the center of the gravitational potential field will be set as the goal of the spacecraft when returning from a distant proximity. In order to keep a stable motion state for the spacecraft, the gravitational potential field center is designed to move along the initial orbit of the spacecraft. In other words, the position state of the nonmaneuvering spacecraft is considered as the center of the gravitational potential field.

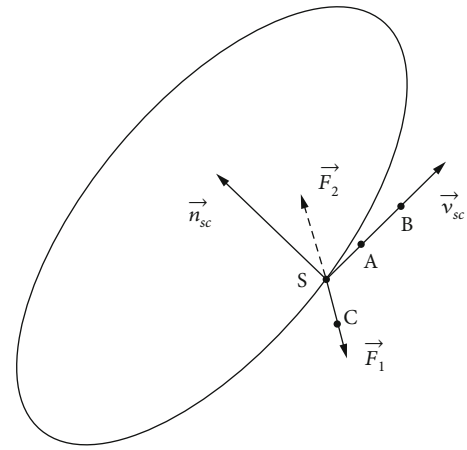

Figure 4: Diagram of the selection of the unit vector direction of the thrust direction.

If the state vector at the initial moment of the spacecraft is $x_0 = (x_0, y_0, z_0, vx_0, vy_0, vz_0)$, the initial state vector of the gravitational potential field center will be x_{a0}. By substituting the initial state vector x_0 into Equation (1), the state vector of the center of the gravitational potential field at the time of t_f will be $x_{\text{af}} = (x_{\text{af}}, y_{\text{af}}, z_{\text{af}}, \text{vx}_{\text{af}}, \text{vy}_{\text{af}}, \text{vz}_{\text{af}})$.

The gravitational potential function $U_{\text{att}}(q)$ is

$$U_{\text{att}}(d_{\text{att}}) = \frac{2}{5} \cdot k_{\text{att}} \cdot \|d_{\text{att}}\|^{2.5} \tag{36}$$

where k_{att} is the gain coefficient of the gravitational potential field, d_{att} is the Euclidean distance between the spacecraft and the center of the gravitational potential field, as defined in Equation (37).

$$d_{\text{att}} = \sqrt{\left(x_f' - x_{\text{af}}\right)^2 + \left(y_f' - y_{\text{af}}\right)^2 + \left(z_f' - z_{\text{af}}\right)^2}, \tag{37}$$

where x_f', y_f', and z_f' represent the location of the spacecraft at the moment of t_f.

Therefore, the gravitation $F_{\text{att}}(d_{\text{att}})$ on the spacecraft is the negative gradient of the repulsive potential field function $U_{\text{att}}(d_{\text{att}})$, denoted as

$$F_{\text{att}}(d_{\text{att}}) = -\nabla U_{\text{att}}(d_{\text{att}}) = -k_{\text{att}} \cdot {d_{\text{att}}}^{1.5}. \tag{38}$$

The result of Equation (38) represents the combined gravitational force on the spacecraft, whose components in the three directions in the ECI coordinate system are distributed according to the unit vector from the spacecraft to the center of the gravitational potential field.

Accordingly, the vector from the spacecraft to the gravitational potential field center is the gravitational direction vector $\overrightarrow{F'_{\text{att}}}$, which is denoted as

$$\overrightarrow{F'_{\text{att}}} = \left(\alpha'_{\text{att}}, \beta'_{\text{att}}, \gamma'_{\text{att}}\right) = \left(x_{\text{af}} - x'_f, y_{\text{af}} - y'_f, z_{\text{af}} - z'_f\right). \quad (39)$$

After normalizing the gravitational direction vector $\overrightarrow{F'_{\text{att}}}$, the unit vector along the gravitational direction is $\overrightarrow{F_{\text{att}}} = (\alpha_{\text{att}}, \beta_{\text{att}}, \gamma_{\text{att}})$, where

$$\begin{cases} \alpha_{\text{att}} = \dfrac{\alpha'_{\text{att}}}{\sqrt{\left(\alpha'_{\text{att}}\right)^2 + \left(\beta'_{\text{att}}\right)^2 + \left(\gamma'_{\text{att}}\right)^2}}, \\ \beta_{att} = \dfrac{\beta'_{\text{att}}}{\sqrt{\left(\alpha'_{\text{att}}\right)^2 + \left(\beta'_{\text{att}}\right)^2 + \left(\gamma'_{\text{att}}\right)^2}}, \\ \gamma_{\text{att}} = \dfrac{\gamma'_{\text{att}}}{\sqrt{\left(\alpha'_{\text{att}}\right)^2 + \left(\beta'_{\text{att}}\right)^2 + \left(\gamma'_{\text{att}}\right)^2}}. \end{cases} \quad (40)$$

According to Equations (38) and (40), the gravitational forces in the three directions of the spacecraft are

$$\begin{cases} F_x = \alpha_{\text{att}} \cdot F_{\text{att}}(d), \\ F_y = \beta_{\text{att}} \cdot F_{\text{att}}(d), \\ F_z = \gamma_{\text{att}} \cdot F_{\text{att}}(d). \end{cases} \quad (41)$$

4.5. Analysis on the Maneuvering Strategy of the Spacecraft at the Stage of Returning from a Close Proximity. Limited by the artificial gravitational potential function, the gravitational force of the spacecraft calculated when approaching the goal may be small, not accurate enough to guarantee the spacecraft return exactly to goal. Therefore, the study on the maneuvering strategy of spacecraft in the close proximity collision avoidance phase uses the PSO algorithm.

For a better description, this section discusses the relative motion model under the CW coordinate system, while the selection of the goal remains the same as those in the previous section. Assuming that the spacecraft enters the stage of returning from a close proximity, the state quantity of the goal and the spacecraft in the ECI coordinate system is $\mathbf{X}_A = [\mathbf{r}_A, \mathbf{v}_A]$ and $\mathbf{X}_A = [\mathbf{r}_B, \mathbf{v}_B]$, respectively. The CW coordinate system takes the coordinates of the target point $\mathbf{r}_A$ as the origin; so, the relative state of the spacecraft relevant to the goal in the CW coordinate system is $\mathbf{X_0} = [\mathbf{r_0}, \mathbf{v_0}]$, where

$$\begin{cases} \mathbf{r_0} = \mathbf{r_B} - \mathbf{r_A}, \\ \mathbf{v_0} = \mathbf{v_B} - \mathbf{v_A} - \dfrac{\mathbf{r_A} \times \mathbf{v_A}}{\mathbf{r_A}^2} \times \mathbf{r_0}. \end{cases} \quad (42)$$

To obtain the current desired output $\mathbf{U}_0$ based on the current state quantity $\mathbf{X}_0$ and the state quantity $\mathbf{X_1}$ at the next moment, deform Equation (10) into

$$\mathbf{U_0} = \mathbf{G^{-1}}(\mathbf{X_1} - \mathbf{\Gamma X_0}) \quad (43)$$

Similarly, the spacecraft's pulse maneuver time interval is T. For any state of the spacecraft at any $t = t_0 + kT$ moment calculated through Equation (12), the output set at each time interval is $\tilde{\mathbf{U}}$,; so,

$$\tilde{\mathbf{U}} = \tilde{\mathbf{\Gamma}}^{-1}\left(\mathbf{X_k} - \mathbf{\Gamma^k X_0}\right), \quad (44)$$

where $\tilde{\boldsymbol{u}} = [\boldsymbol{u}_0, \boldsymbol{u}_1, \cdots, \boldsymbol{u}_{N-1}]^T$.

Assuming that the spacecraft needs a total of Npulses to complete the mission, to reach the goal step-by-step, an optimization model for the spacecraft reaching the goal will be built as

$$s.t.\{0 \le \mathbf{u}_k \le u_{\max}\}. \quad (45)$$

In the model, ${}^{S,P}D_k$ denotes the distance to the goal at the k-th pulse of the spacecraft, $\mathbf{u}_k$ denotes the 2-norm of the pulse vector at the k-th maneuver of the spacecraft, $u_{\max}$ denotes the maximum input control that can be generated by the spacecraft, and α_1 and α_2 are weighting factors.

To study the maneuver strategy of the spacecraft in respect of returning to the goal, the particles in the PSO algorithm are given actual physical meanings. Each particle position represents a possible location where the spacecraft might reach. Based on that, the solution of the particle after PSO optimization will be a node along the maneuvering path of the spacecraft. Through Equation (45), the optimal value searched by each particle in the particle swarm exchanges information, and the optimal value produced in every search will be the end position of the motion path for spacecraft at this moment. The search process will not stop repeating until it reaches the goal. The Equation (43) calculates the pulse velocity increment at each moment while the spacecraft is moving to the goal.

To update the velocity and position of each particle in the PSO algorithm, the equation is

$$\begin{cases} v_{i,d}^{k+1} = \omega v_{i,d}^k + c_1 r_1\left(p_{i,d}^k - x_{i,d}^k\right) + c_2 r_2\left(p_{g,d}^k - x_{i,d}^k\right), \\ x_{i,d}^{k+1} = x_{i,d}^k + v_{i,d}^{k+1}, \end{cases} \quad (46)$$

where the physical meaning of symbols in the equation is as shown in Table 1.

The inertia weight ω is important for particle convergence and mitigating the contradiction between particle swarm search and exploitation. A larger ω is helpful to increase the diversity of the swarm, while a smaller ω is beneficial for the exploitation of local optima. When planning the return path of the spacecraft to the goal, the ω requires specifically settings: at the initial stage, a larger search range is needed for spacecraft to quickly approach the goal; however, when the spacecraft is approximate to the goal, local

optimum solution can be produced by searching in a smaller range, thus reducing the repeated oscillations. To enhance the search rate and accuracy, the study adopts the inertia weights dynamically changing:

$$\omega = \omega \frac{k_{\max}}{k_{\max}(\omega \min_{\max})_{\min}}, \tag{47}$$

where $\omega_{\min}$ represents the minimum inertia weight, $\omega_{\max}$ is the maximum inertia weight, k is the number of current iterations, and $k_{\max}$ is the maximum times of iterations.

Suppose $f(\cdot)$ denotes the fitness function and $n_p n_p$ is the number of particles in the particle swarm, to find the minimal value, the individual optimal position $p_{i,d}^k p_{i,d}^k$ for the first k iterations of the $i_^{\text{th}}$ particle is calculated in the equation:

$$p_{i,d}^{k+1} = \begin{cases} p_{i,d}^k, iff\left(x_{i,d}^{k+1}\right) \geq f\left(p_{i,d}^k\right), \\ x_{i,d}^{k+1}, iff\left(x_{i,d}^{k+1}\right) < f\left(p_{i,d}^k\right). \end{cases} \tag{48}$$

For the global optimal position $p_{g,d}^k$ in the first k iterations of all particles, the equation is

$$\begin{aligned} p_{g,d}^k \in \left\{ \left(p_{1,d}^k, p_{2,d}^k, \cdots, p_{n_p,d}^k\right) \middle| f\left(p_{g,d}^k\right) \right. \\ \left. = \min\left\{ f\left(p_{1,d}^k\right), f\left(p_{2,d}^k\right), \cdots, f\left(p_{n_p,d}^k\right) \right\} \right\}. \end{aligned} \tag{49}$$

When the velocity of the particle swarm is updating, it might be very large, even causing the particles to rush out of the solution range or even diverge. In order to control the search action of each particle, the particle flight speed has to be controlled within a specific range. Therefore, the particle velocity equation will be updated as

$$v_{i,d}^{k+1} = \begin{cases} v_{i,d}^{k+1}, \text{if} \left| v_{i,d}^{k+1} \right| \leq V_{\max,d}, \\ V_{\max,d}, if\, v_{i,d}^{k+1} > V_{\max,d}, \\ -V_{\max,d}, if\, v_{i,d}^{k+1} < -V_{\max,d}, \end{cases} \tag{50}$$

where $V_{\max,d}$ is the maximum velocity that a particle can have in the $d_^{\text{th}}$ dimension.

Since the search distance of particle swarm is usually restricted to certain constraints, for example, at the initial search moment of the PSO algorithm, it is expected that a larger search radius can motivate the random walk of particles. As the spacecraft approaches the goal, a larger search radius may lead to a large computational cost caused by the PSO algorithm when converging to the goal.

As a result, this paper constrains the initial values of each particle in the swarm to a sphere region with radius of R_{PSO}. The position of the sphere center is determined by the position information of the spacecraft at the moment, while the radius of the sphere is depending on the distance between the spacecraft and the corresponding goal. In this paper, the radius is proportional to the distance between the spacecraft and the goal. The radius of the particle swarm algorithm search sphere is R_{PSO}; so,

$$R_{\text{PSO}} = \frac{\beta_1}{1 + e^{-\left(\beta_2 \cdot^{S.P} D_k + \beta_3\right)}} + \beta_4, \tag{51}$$

where $\beta_1 \boxtimes \beta_2 \boxtimes \beta_3 \boxtimes \beta_4$ are coefficients.

It should be noted that the particles in the PSO algorithm might move out of the search radius of the particle swarm when performing random walk; so, boundary treatment is also needed.

As shown in Figure 5, if the spacecraft is located at A, at the time t, the sphere represents the search range of PSO algorithm. If a location B is searched by particle i in the swarm, it indicates that the particle has reached beyond the search boundary of the particle swarm, requiring boundary treatment. In order to reduce the influence of the treatment on the iterations and evolutionary direction of the particle swarm, this paper contracts the position of particle i along the vector $\overrightarrow{AB}$ and corrects the location of particle i from point B to point B'.

Suppose the coordinates of points are (x_1, y_1, z_1), (x_2, y_2, z_2), and $B' = (a, b, c)(x_2, y_2, z_2)$, then the unit vector $\boldsymbol{\eta} = [\eta_x, \eta_y, \eta_z]$ of vector $\overrightarrow{\text{AB}}$ is

$$\begin{cases} \eta_x = \dfrac{x_2 - x_1}{\sqrt{(x_2 - x_1)^2 + (y_2 - y_1)^2 + (z_2 - z_1)^2}}, \\ \eta_y = \dfrac{y_2 - y_1}{\sqrt{(x_2 - x_1)^2 + (y_2 - y_1)^2 + (z_2 - z_1)^2}}, \\ \eta_z = \dfrac{z_2 - z_1}{\sqrt{(x_2 - x_1)^2 + (y_2 - y_1)^2 + (z_2 - z_1)^2}}. \end{cases} \tag{52}$$

As $\overrightarrow{OB'} = \overrightarrow{OA} + \overrightarrow{AB'}$,, the modified coordinates of the particles are

$$\begin{cases} a = x_1 + \eta_x \cdot R_{\text{PSO},} \\ b = x_2 + \eta_y \cdot R_{\text{PSO}}, \\ c = x_3 + \eta_z \cdot R_{\text{PSO}.} \end{cases} \tag{53}$$

Figure 6 shows the PSO search path used by the spacecraft. In conclusion, at the moment of $t_0 t_0$, the spacecraft is at the initial position, which is taken as the sphere center. In this sphere with the radius of R_0, n_p particles are randomly generated. The global optimal particle position will be selected as the spacecraft position at $t_0 + T$ after $k_{\max}$ iterations. Based on this and repeat the computation, we can plan the tracking and return path of the spacecraft to the goal.

5. Simulation Analysis

The analysis first used the NASA EVOLVE 4.0 model to simulate the generation of space debris group. Table 2 shows

Table 1: Physical meaning of symbols in Equation (46).

Symbol	Meaning
i	Particle number
k	The times of current iterations
d	The dimension of the solution
$v_{i,d}^{k}$	Velocity information of the $i_^{\text{th}}$ particle on the $d_^{\text{th}}$ dimensional solution at the $k_^{\text{th}}$ iteration
$x_{i,d}^{k}$	The position of the $i_^{\text{th}}$ particle on the d dimensional solution at the $k_^{\text{th}}$ iteration
$p_{i,d}^{k}$	The individual optimal position of the $i_^{\text{th}}$ particle for the previous k iterations
$p_{g,d}^{k}$	The global optimal positions of all particles for the previous k iterations
ω	Inertia weights
c_1, c_2	Nonnegative constants
r_1, r_2	Any constants between [0,1]

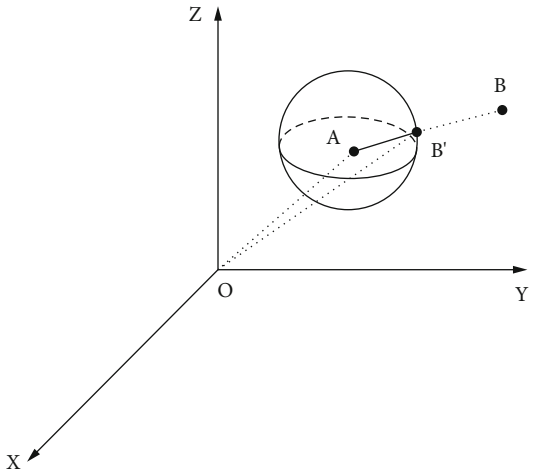

Figure 5: Diagram of modifying particles that are beyond the search range.

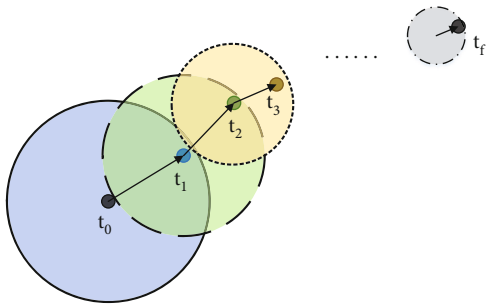

Figure 6: Diagram of the Spacecraft Using PSO Algorithm to Search the Path.

the six orbital elements of the active spacecraft at the initial stage and of the spacecraft that are disintegrating.

The disintegrating spacecraft spawns space debris group disintegration point, creating a total of 15,573 pieces of debris, while debris less than 0.5 g are not counted in the analysis. The circle center of the unreachable domain is (42014, 0, 0) km with a radius of 158 km.

The mass of the active spacecraft is 1000 kg, the spacecraft thrust is no more than 100 N, the repulsive potential field gain coefficient k_{rep} is 100, taken from the upper limit of spacecraft thrust, and the repulsive potential field action range is $d_0 = 3000$km.

At the stage of avoidance and the stage of returning from the distant proximity, the thrust magnitude in the three directions and total thrust of the spacecraft are as shown in Figure 7. It should be noted that the thrust and the acceleration are in different directions, indicating that the spacecraft is under the repulsive potential field from 173 to 1200 seconds and under the gravitational potential field from 1200 to 2446 seconds.

In Figure 7, the spacecraft is less than 3000 km away from the unreachable domain at about 173 seconds when entering the stage of avoidance. At this timestamp, the artificial repulsion function is used to make the spacecraft gradually move away from the no-fly zone, during which the spacecraft enters the stage of approaching from the distant proximity from 1200 seconds to 2446 seconds. By then, the artificial gravitational function enables the spacecraft to obtain a gravity pointing at the target point, thus gradually approaching the goal. Limited by the artificial potential function, the distance between the spacecraft and the goal is the shortest at 2446 seconds when the gravity provided by the gravitational potential field is insufficient to pull the spacecraft back to the goal in such a short distance. After that, the spacecraft enters the stage of returning from the stage of close proximity.

It is worth mentioning that when the active spacecraft enters the stage of returning from the distant proximity, the spacecraft's initial velocity is too big for the gravity calculated with the gravitational potential field function to change the spacecraft's motion trend in a short period of time. As a result, the distance between the spacecraft and the target point will gradually extend at the beginning stage of avoiding from a distant proximity. Until about 1679 seconds, the gravity is sufficient to change the moving direction of the spacecraft, leading the spacecraft to approach the goal. Therefore, between 1200 and 1679 seconds, although the spacecraft is provided with a thrust pointing towards the

Table 2: The six elements of initial moment active spacecraft and disintegrating spacecraft disintegrating moment orbit.

	Active spacecraft	Disintegrating spacecraft
Semimajor axis/km	42164	42014
Eccentricity	0	0
Inclination/°	15	60
Right ascension of the ascending node/°	0	0
Argument of perigee/°	38	245
True anomaly/°	316	142

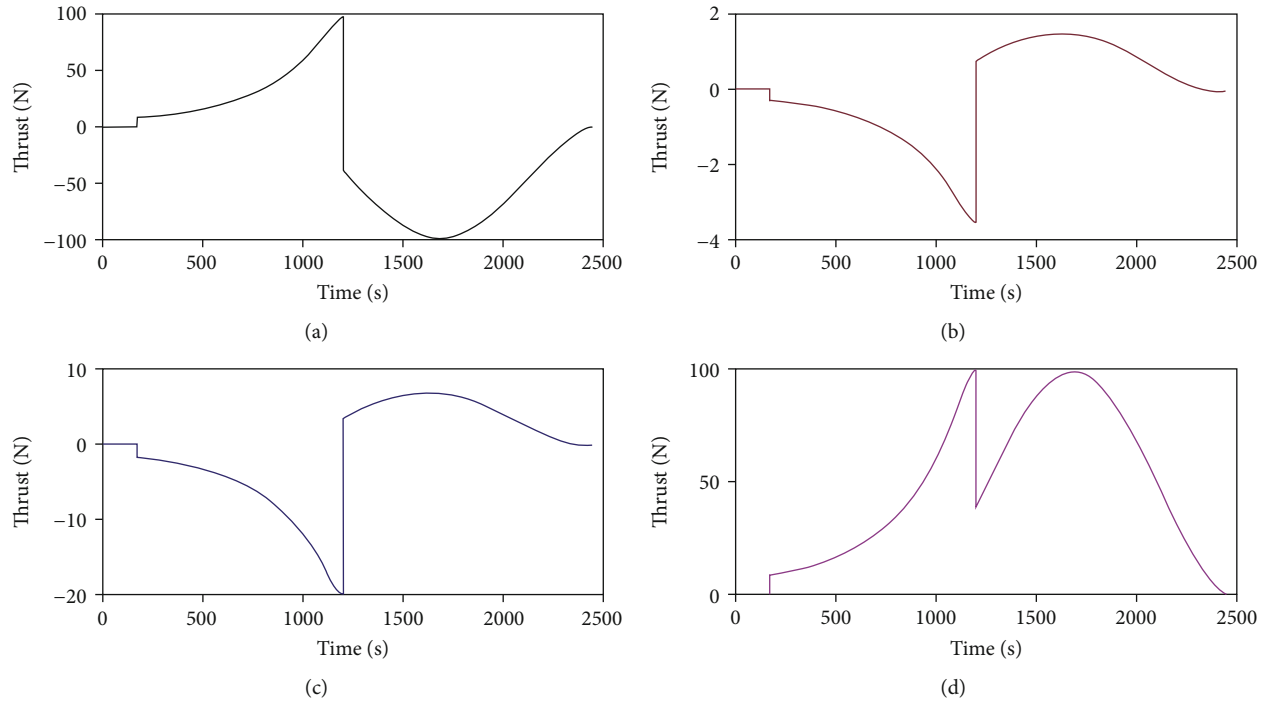

Figure 7: The thrust of the active spacecraft at the stage of avoidance and the stage of returning from the distant proximity: (a) thrust in the X direction, (b) thrust in the Y direction, (c) thrust in the Z direction, and (d) total thrust (scalar).

goal (which is the gravity generated by the artificial gravitational potential field), it moves away from the goal at a decreasing speed until the 1679 seconds when the spacecraft stops to approach the goal.

Figure 8 shows the schematic diagram of the active spacecraft transferring orbit with modified artificial potential field method. The diagram covers the stage of avoidance and the stage of returning from a distant proximity.

Figure 9 shows how the distance between the active spacecraft, and the unreachable domain varies during the maneuver, while Figure 10 illustrates how the distance between the active spacecraft and the goal changes.

In Figure 9, the closest distance between the active spacecraft and the unreachable domain is about 3.3 km; so, there is no risk of collision. As shown in Figure 10, the active spacecraft enters the stage of avoidance from 173 seconds to 1200 seconds, but it gradually moves away from the goal due to the impact of repulsive potential field. Following the stage from 1200 to 2446 seconds, the active spacecraft is under the gravitational potential field. However, during 1200 to 1679 seconds, the large inertia of the spacecraft prevents its motion state from an instant change caused by the gravitational potential field. As the spacecraft continues to move towards the goal, the distance between the spacecraft and the goal continues increasing. In spite of this, the increasing speed gradually slows down. At the 1679 seconds, the gravitational potential field has offset the inertia of the original motion when the spacecraft stops moving away from the goal but starts to approach the target. Afterwards, the distance between the spacecraft and the target narrows to the minimum at 2446 seconds when the spacecraft ends its stage of returning from the distant proximity.

At 2446 seconds, the spacecraft will enter the stage of returning from a close proximity. The states of the spacecraft and the goal under the ECI coordinate system at the time are shown in Table 3.

The CW coordinate system is established with the goal as the center of the circle. Substituting the initial values of

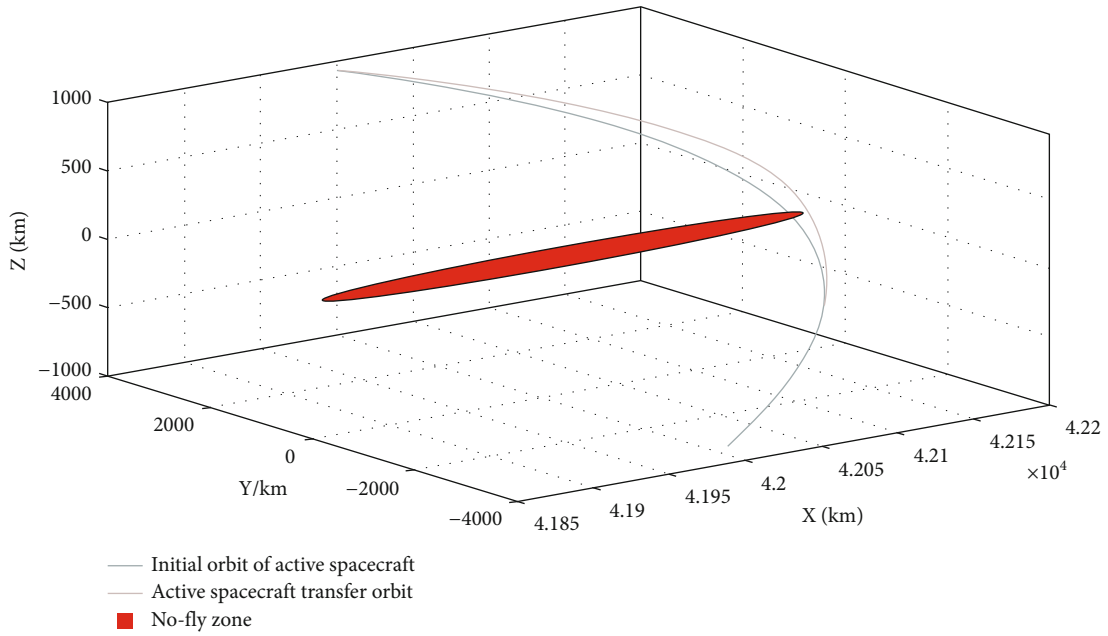

Figure 8: Active spacecraft transfers orbit based on the modified artificial potential field method.

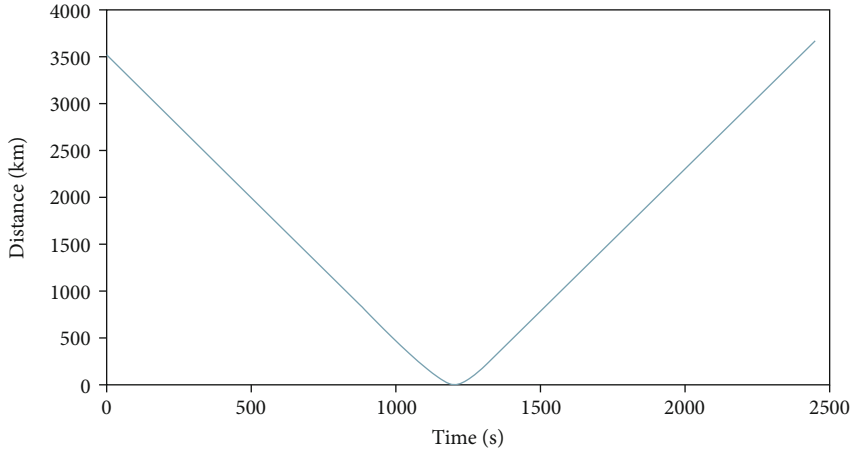

Figure 9: The variation of distance between active spacecraft and unreachable domain.

the states in Table 3 into Equation (42), the initial states of the spacecraft relative to the goal under the CW coordinate system is shown in Table 4.

It should be noted that since the CW coordinate system is established with the goal's position as the circle center, the state of the goal's position is $[0, 0, 0]$.

Subsequently, the PSO algorithm carries out the simulation analysis on the path planning of the active spacecraft, and parameter values used in the PSO algorithm are

$$n_p = 100, c_1 = 2, c_2 = 2, V_{\max} = 10, d = 3,$$
$$k_{\max} = 100, \omega_{\min} = 0.3, \omega_{\max} = 0.75. \quad (54)$$

For the search radius of the particle swarm, given $\beta_1 = 80$, $\beta_2 = 0.02$, $\beta_2 = 0.02$, $\beta_3 = 0$, and $\beta_4 = -39$, the relationship between spacecraft-goal distance and the particle swarm search radius is as shown in Figure 11.

In Equation (45), for the function to be optimized, the parameters are $\alpha_1 = 0.8$ and $\alpha_2 = 0.2$. The maximum pulse maneuvering volume for each maneuver of the spacecraft is defined as $\Delta u < 20$m/s. In the simulation, the spacecraft performs pulse maneuvering at a time interval of 1 second. It takes the calculation of pulse maneuvering size and direction for about 0.48 seconds per time on average, while the maximum time is about 0.52 seconds, meeting the real-time requirements of the mission.

The PSO algorithm also solves the maneuver mode and movement trajectory of the spacecraft in each iteration, and the results are shown in Figures 12–14. Figure 12 shows the trajectory of the spacecraft to the goal, Figure 13 demonstrates the variation curve of distance between the spacecraft and the goal, and Figure 14 illustrates the spacecraft's total

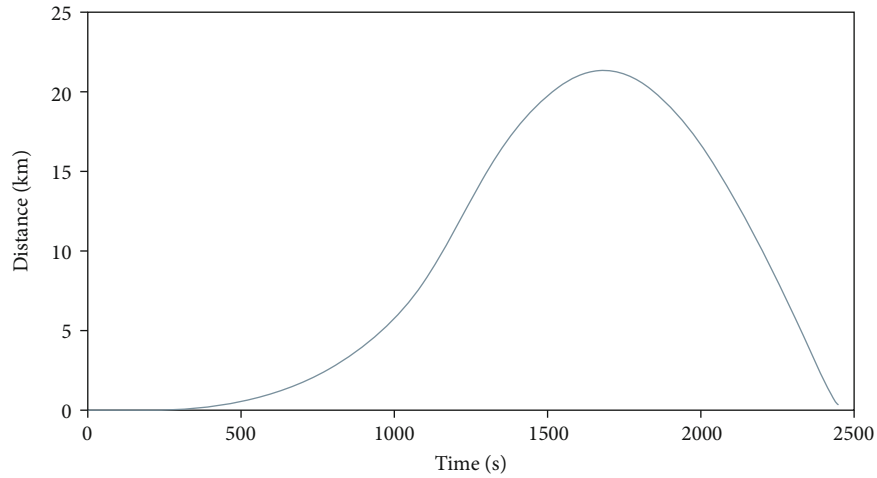

Figure 10: The variation of distance between the active spacecraft and the goal.

Table 3: States of the spacecraft and the goal under the ECI coordinate system at the initial moment of the stage of returning from a close proximity.

	x/m	y/m	z/m	$v_x/\mathrm{m}\cdot\mathrm{s}^{-1}$	$v_y/\mathrm{m}\cdot\mathrm{s}^{-1}$	$v_z/\mathrm{m}\cdot\mathrm{s}^{-1}$
Spacecraft	41990424.042	3692364.155	989081.845	-319.571	-319.571	-319.571
Goal	41990353.815	3692445.699	989387.824	-278.757	-278.757	-278.757

Table 4: The state of the spacecraft relative to the goal in the CW coordinate system at the initial moment of the stage of returning from the close proximity.

	x/m	y/m	z/m	$v_x/\mathrm{m}\cdot\mathrm{s}^{-1}$	$v_y/\mathrm{m}\cdot\mathrm{s}^{-1}$	$v_z/\mathrm{m}\cdot\mathrm{s}^{-1}$
Relative state	70.227	-81.544	-305.978	-40.826	-0.680	-2.963

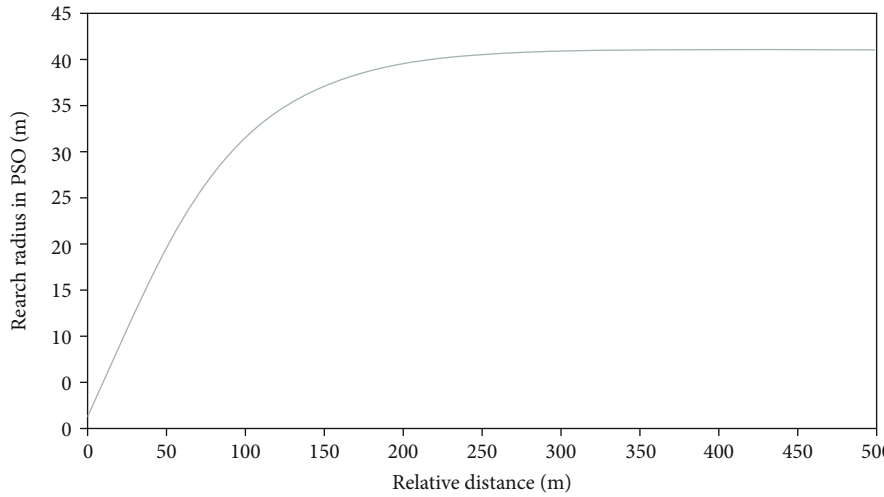

Figure 11: Relationship between the spacecraft-goal distance and the particle swarm search radius.

pulse of the orbital maneuver at the stage of approaching from the close proximity.

As shown in Figures 12 and 13, the PSO algorithm searches radius with dynamic variation helping the spacecraft return to the goal in about 13 seconds, thus effectively transferring the original orbit of returning from a close proximity. It should be noted that as the initial velocity of the spacecraft relative to the goal is too large, the motion curve of the spacecraft might not be smooth at the initial stage. The relative distance between the spacecraft and the goal

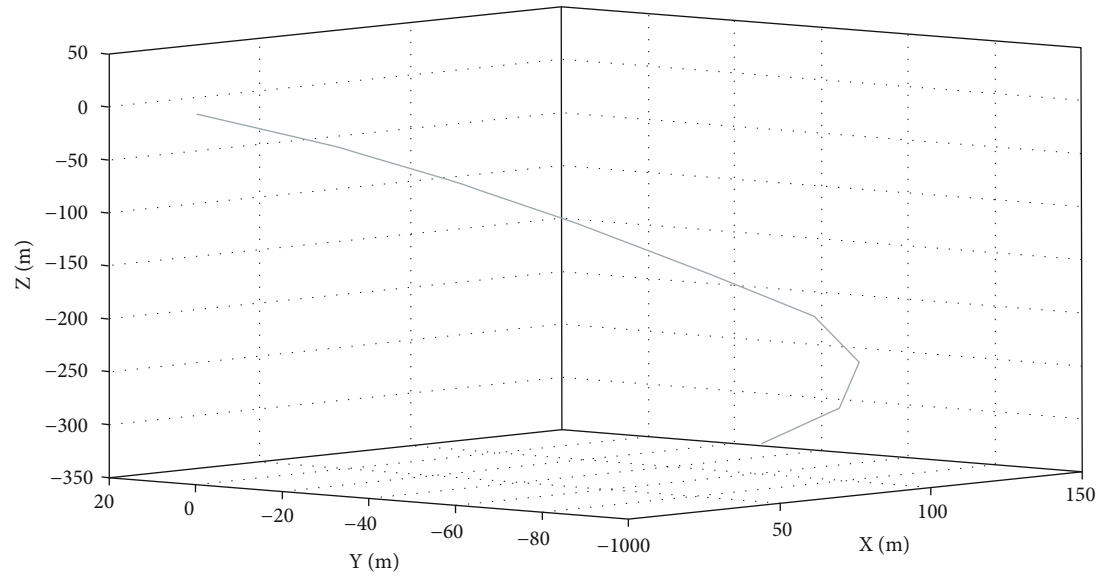

Figure 12: The trajectory of the spacecraft to the goal.

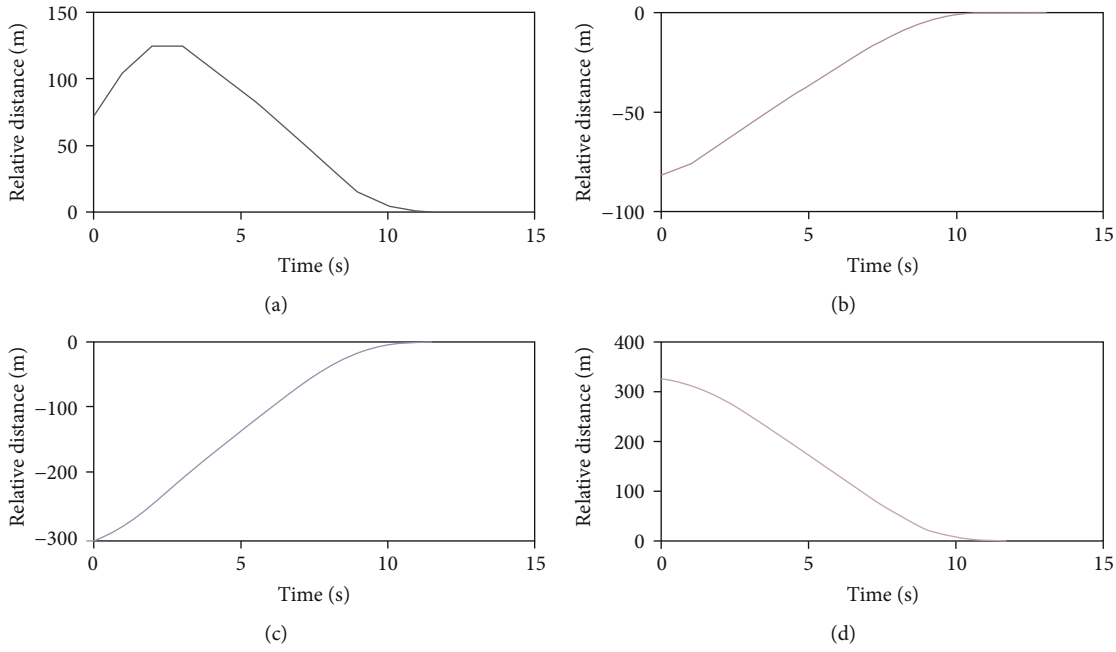

Figure 13: The distance between the spacecraft and the goal: (a) distance in the X direction, (b) distance in the Y direction, (c) distance in the Z direction, and (d) total distance.

in the $O'X'$ direction of the CW coordinate system increases before shrinking. However, in Figure 14, maneuver pulse amount is always less than 20 m/s during the process of the spacecraft maneuvering.

As shown in Figure 13, both the spacecraft-goal distance and velocity are close to 0 at about 13 seconds. Similarly in Figure 14, the pulse amount required for orbital maneuvers is around 0 after 13 seconds. Based on the two conditions above, the improved PSO algorithm can successfully push the spacecraft to back to its original orbit at about 13 seconds; so, no further maneuvers will be needed afterwards. As a result, the spacecraft is managed to continue its flight along its original orbit while being successfully prevented from the collision with the debris group.

To sum up, this paper proposes an effective maneuver strategy for spacecraft to avoid space debris group and return to the original orbit. In existing studies, studies on how spacecraft evade space debris groups are not sufficient, as most research focuses on space debris. The simulation analysis effectively describes the unreachable domain of the space debris group by reducing the dimensionality of the changing geometry configuration of the space debris group. To calculate the avoidance orbit and return orbit of spacecraft, the APF method and PSO algorithm are adopted in

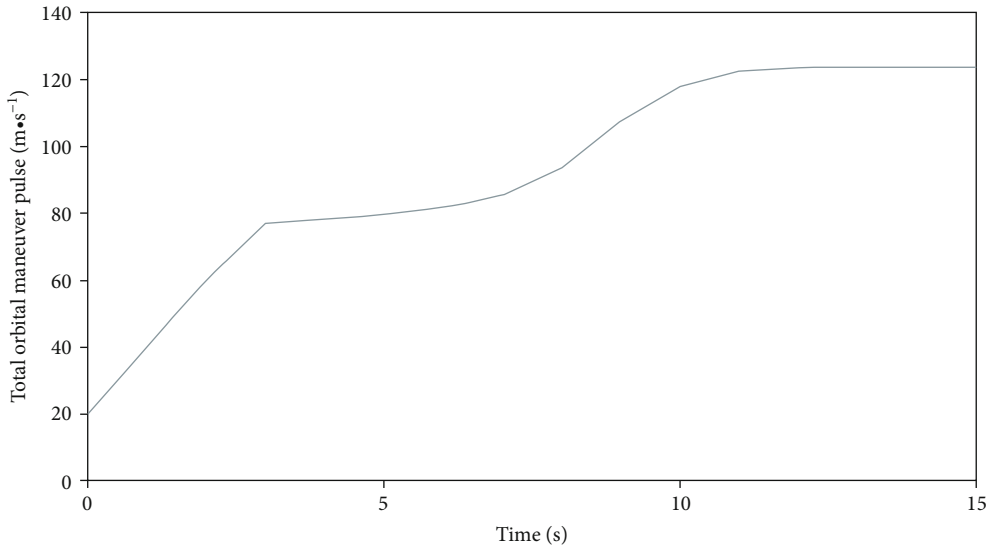

Figure 14: The time variation curve of the spacecraft's total orbital maneuver pulse at the stage of approaching from a close proximity.

the analysis. During the process, the APF method and PSO algorithm are improved. The APF method is suitable for spacecraft with high velocity by distance projection, while the calculation efficiency of the PSO algorithm is improved by dynamic searching radius.

6. Conclusions

This paper proposes a method of orbital transfer for spacecraft to urgently avoid the debris group in the near space and return to its original orbit. The method innovatively highlights the following: (1) the changing geometry of the space debris group is simplified by dimensionality reduction while the mathematical method describes the space debris group as an unreachable domain, (2) the method figures out a maneuver strategy covering three stages from avoidance to return, (3) the method suggests to use distance projection approach to break the limitations of the artificial repulsive potential function based on the special features of the spacecraft motion at the stage of avoidance, and (4) the method proposes a modified function to search with dynamic changing search radius and particle correction approach for a spacecraft at the stage of returning from a close proximity, which ensures the random walk of the PSO algorithm in the initial phase and the computational efficiency in the ending phase, to avoid local oscillation.

Data Availability

The data used to support the findings of this study are included within the article.

Conflicts of Interest

The authors declared that they have no conflicts of interest in this work.

References

[1] ESA, "Space debris by the numbers," 2021, https://www.esa.int/Safety_Security/Space_Debris/Space_debris_by_the_numbers.

[2] C. Pardini and L. Anselmo, "Review of past on-orbit collisions among cataloged objects and examination of the catastrophic fragmentation concept," *Acta Astronautica*, vol. 100, pp. 30–39, 2014.

[3] P. D. Anz-Meador, J. Opiela, D. Shoots, and J. C. Liou, *History of on-orbit satellite fragmentations*, National Aeronautics and Space Administration Johnson Space Center Orbital Debris Program Office, 2018.

[4] T. Wang, "Analysis of debris from the collision of the cosmos 2251 and the iridium 33 satellites," *Science & Global Security*, vol. 18, no. 2, pp. 87–118, 2010.

[5] C. Pardini and L. Anselmo, "Physical properties and long-term evolution of the debris clouds produced by two catastrophic collisions in Earth orbit," *Advances in Space Research*, vol. 48, no. 3, pp. 557–569, 2011.

[6] J. C. Liou, "Collision activities in the future orbital debris environment," *Advances in Space Research*, vol. 38, no. 9, pp. 2102–2106, 2006.

[7] Y. L. Zhang and Z. K. Wang, "Space traffic safety management and control," *IEEE Transactions on Intelligent Transportation Systems*, vol. 17, no. 4, pp. 1189–1192, 2016.

[8] P. Russell, "Space vehicle conflict-avoidance analysis," *Journal of Guidance, Control, and Dynamics*, vol. 30, no. 2, pp. 492–498, 2007.

[9] K. Chan, "Spacecraft maneuvers to mitigate potential collision threats," *AIAA/AAS Astrodynamics Specialist Conference and Exhibit*, vol. 4629, 2002.

[10] S. Alfano, "Collision avoidance maneuver planning tool," in *15th AAS/AIAA Astrodynamics Specialist Conference*, pp. 7–11, Lake Tahoe, California, 2005.

[11] J. B. Mueller, P. R. Griesemer, and S. J. Thomas, "Avoidance maneuver planning incorporating station-keeping constraints and automatic relaxation," *Journal of Aerospace Information Systems*, vol. 10, no. 6, pp. 306–322, 2013.

[12] J. B. Mueller, "Onboard planning of collision avoidance maneuvers using robust optimization," in *AIAA Infotech at Aerospace Conference and Exhibit and AIAA Unmanned … Unlimited Conference*, p. 2051, Seattle, Washington, 2009.

[13] M. Graziano, F. Pirondini, N. Sánchez, and E. Di Sotto, "CryoSat collision warning and low thrust avoidance manoeuvre strategy," *European Space Agency-Publications-ESA SP*, vol. 473, pp. 455–462, 2001.

[14] B. Kelly and S. De Picciotto, "Probability based optimal collision avoidance maneuvers," *Spaceflight*, vol. 2005, p. 6775, 2005.

[15] J. L. Gonzalo, C. Colombo, and P. D. Lizia, "Analysis and design of collision avoidance maneuvers for passive deorbiting missions," in *AAS/AIAA Astrodynamics Specialist Conference*, pp. 2189–2208, Snowbird, UT, USA, 2018.

[16] J. L. Gonzalo, C. Colombo, and P. D. Lizia, "A semi-analytical approach to low-thrust collision avoidance manoeuvre design," in *70th International Astronautical Congress*, Washington, DC, 2019.

[17] J. L. Gonzalo, C. Colombo, and P. D. Lizia, "Introducing MISS, a new tool for collision avoidance analysis and design," *Journal of Space Safety Engineering*, vol. 7, no. 3, pp. 282–289, 2020.

[18] Y. L. Zhang, B. B. Zhang, and Z. K. Wang, "Long-term evolution modeling method of space debris environment," *Journal of Astronautics*, vol. 39, no. 12, pp. 1408–1418, 2018.

[19] K. Dharmarajan, G. E. Palmerini, and M. Sabatini, "Collision avoidance for satellites in formation flying," *Advances in Astronautical Sciences*, vol. 173, pp. 24–37, 2020.

[20] H. Curtis, *Orbital Mechanics for Engineering Students*, Butterworth-Heinemann, 2014.

[21] N. L. Johnson, P. H. Krisko, J. C. Liou, and P. D. Anz-Meador, "NASA's new breakup model of evolve 4.0," *Advances in Space Research*, vol. 28, no. 9, pp. 1377–1384, 2001.

[22] S. Frey and C. Colombo, "Transformation of satellite breakup distribution for probabilistic orbital collision hazard analysis," *Journal of Guidance, Control, and Dynamics*, vol. 44, no. 1, pp. 88–105, 2021.